

Finite Element Methods for a Class of Interface Problems

275395

Contents

1	Introduction	2
1.1	Overview	2
1.2	Aims	3
2	Rheology of a suspension of particles	4
2.1	Einstein model [1906]	4
2.2	Brinkman [1952]	4
2.3	Krieger & Dougherty [1959]	5
3	Phase-change Boussinesq models	5
3.1	Main assumptions and model equations	5
3.2	Enthalpy-Porosity models for phase change	6
3.3	Enthalpy-Viscosity model for phase change	6
3.4	Weak formulation	7
3.5	Stability analysis	8
4	Finite element scheme	13
4.1	A finite element method	14
4.2	Consistent linearisation	15
5	Numerical tests	16
5.1	Experimental convergence for the semidiscrete and fully discrete methods	16
5.2	Benchmark test: natural convection of air	17
6	The Melting of n-Octadecane	19
6.1	The Enthalpy-Viscosity method	20
6.2	The Enthalpy-Porosity method	20
6.3	Numerical results	20
7	Different Mushy Region sizes for the Enthalpy-Viscosity method	21

8	Jump forms arising from literature	23
8.1	Carman-Kozeny form	23
8.2	New Viscosity model	23
9	Intuition on the modelling	25
9.1	Local Element	25
9.2	Similarity between forms	26
10	Modelling restrictions, and future modelling	26
10.1	Viscosity Formulation, application; Mantle Convection	26
10.2	Increasing sensitive parameter and the limitation of the finite element method; Plane Wing	27
10.3	Rayleigh Taylor instability	28
10.4	Antarctica	29
11	Conclusion	30
12	References	30
13	Appendix	32
13.1	Appendix A	32
13.2	Appendix B	33

1. Introduction

1.1. Overview

Firstly, I review literature on how imposing particles in a fluid affects the viscosity of the solution. The Boussinesq system is introduced and we present two different models that can embed a phase change, the Enthalpy-Viscosity and the Enthalpy-Porosity model. The weak formulation of the Boussinesq system is introduced, stability and uniqueness results are presented. We then introduce the finite element formulation, and the methodology used to solve the numerical problem. The formulation is verified with two numerical benchmarks.

Secondly, we turn our attention to the numerical modelling of the Enthalpy-Viscosity and Enthalpy-Porosity models of phase change, by means of simulating the melting n-Octadecane using an almost identical jump function that imposes the change of phase. The models have not been compared in literature, and the results between the models are notably different. We then identify a parameter that has a more profound effect on the model than one might suspect and produce some numerical results that suggests that the difference observed between the two models of phase change could be remedied.

Thirdly, we numerically model the Carman-Kozeny jump form for porosity, and a new jump form for viscosity inspired by literature discussed in the first section. The viscosity form introduced has never been made temperature dependent to embed a phase change so is new to the literature of phase change. We show that it can produce good results and how this model can also resolve the difference observed between the Enthalpy-Viscosity method and the Enthalpy-Porosity method.

We discuss further the modelling by a novel numerical model, where we embed a phase change by introducing a mesh that imposes fixed particles in a solid region. This is done to illustrate the context in which the Carman-Kozeny form arises, and how it differs from the introduced viscosity formulation.

Finally, a less formal section on future exploration of this research topic is presented. We discuss limitation of the model and other modelling issues by means of numerical examples relating to physical models, it is lighter and more brief in nature as the main aims of the project have already been addressed.

1.2. Aims

We put particular focus on how the concentration of nano-particles effects the viscosity of a particle-fluid suspension, as it is less common in the literature on phase change.

In this project we primarily investigate Boussinesq phase change models. Where there is natural convection driven by temperature differences and also a phase change.

In this project we investigate two different methods of imposing phase change. Phase change has been traditionally modelled by the Enthalpy-Porosity model [32] where a jump function inspired by the Carman-Kozeny equation imposes a large drag force in the solid. Phase change has also been modelled by embedding a jump function into the viscosity, see [14]. This project presents the first comparison between these two phase change models.

We also derive a weak formulation of the governing equations and outline a solvability and stability analysis. In Section 4 we introduce a finite element method based on the primal velocity-pressure-temperature formulation of the model. We specify the fully discrete implicit scheme and write down the corresponding Newton linearisation. Next, in Section 5 we present several tests serving as numerical validation for the enthalpy-free case.

To compare these models we implement them on the same numerical example in which a phase change material (n-Octadecane) is melted. We use very similar regularised jump functions of a simple form for both models but observe different results. We then identify an important parameter that allows the observed difference between the two models of phase change to be remedied. The comparison between the two methods of embedding phase change is unique to the literature, and so is the remedy of the difference. This result allows mathematicians or people the ability to change between the two models of phase change, this has utility in not only numerical modelling but also allows the functional analysis to be done on a different system of equations.

We create a physically motivated viscosity formulation, similarly to how the porosity model is considered, in terms of imposing micro particles into the solid. We extract the form for a viscosity jump from the literature on nano-particle suspensions, and although the model exists already, it has only been used in natural convection problems with a fixed small concentration of nano-particle suspension. We present the case for coupling the temperature to the nano-particle concentration in the fluid, and this allows us to create a viscosity embedded phase change model, with the jump form arising from a physical model. We then show that the form can be modified to give us the same result as the Enthalpy Porosity model. We show how micro-structure imposes the correct modelling assumptions, using a local element, and conclude the section.

We then have a final section, that implements the methodology to some numerical examples, with light discussion. We first present a case for the enthalpy viscosity method to embed a phase change for modelling mantle convection, with a new form inspired by experimentation. We then highlight how models can be sensitive to parameter choices, and how the finite element methods can break down, we do this with the introduction of a simple slow flow past an air-foil. We then discuss Rayleigh-Taylor instability. We present the case to show how small perturbations can escalate chaotically, and also introduce the concept of double diffusive convection which we will need for the last model. The last model is a Boussinesq phase change system, for the flow around Antarctica,

as an ice sheet melts. We note that the methods developed in this paper could theoretically model such a system, the factor that stops the progression is the computational power needed to solve the arising linear system. We then present an illustration for a 2d version of the model.

2. Rheology of a suspension of particles

This sub section concerns itself with the viscosity of a fluid in which small particles are suspended in solution. We introduce historical models, in which the viscosity is written as a function of particle concentration. We are seeking a form which we can make dependent on temperature to embed a phase change.

2.1. Einstein model [1906]

We concern ourselves with the viscosity of solutions with suspended particles. We will first introduce the notation with regards to the model introduced in [19] where the relation,

$$\mu = 1 + B\Phi,$$

is postulated, where μ is the relative viscosity, $B = 2.5$ is a theoretical constant called the Einstein coefficient, and Φ is the ratio of the volume of the particles to the volume of the liquid and belongs in the range $[0, 1]$. This model can be derived by the consideration of slow flow past a sphere, and was extended to a sparse packing of equal size hard spherical particles, with no particle-particle interactions [20]. This model corresponds to linear Newton rheology, and is only valid for very dilute suspensions ($\Phi \lesssim 0.01$) [34]. This is not suitable for a phase change model as we want to consider the whole range of Φ .

2.2. Brinkman [1952]

Both Brinkman [7] and Roscoe [31] independently extend the Einstein model to

$$\mu = (1 - \Phi)^{-2.5},$$

using particles of varying sizes. Not only does the binomial expansion match the Einstein form to linear order (matching it closely for small Φ), it captures the property that the viscosity tends to infinity as the ratio of solid volume to total volume tends to 1. This form deals much better with the non Newtonian viscosities observed at higher Φ , than the Einstein model. A derivation from first principles can be found [7], similarly the Carman-Kozeny equation can be determined from just considering the flow past spheres. We compare these two models of phase change later in this project so the fact that both models have derivations from micro-structure is in my opinion interesting.

This form of the viscosity model is currently used in the literature of nano particles, [20], and will be the basis we use for our model of phase change. Traditionally, these models incorporate differences in density and enthalpy by considering nano-particles made of different materials. See for instance [18], where thermal and density properties of copper nano-particles are taken into account. In this context, our model consider nano-particles with the same density and thermal properties. Another important distinction is traditionally these models have a constant concentration of nano-particles whereas in our model the concentration of nano-particles will be made dependent on temperature in such a way that the particles are not present in the liquid phase, and they exhibit maximum concentration in the solid phase.

2.3. Krieger & Dougherty [1959]

Roscoe later goes on to introduce the concept of a critical fraction, where packing density becomes high enough that the fluid behaves as a solid for $\Phi \approx \Phi_m$, so the model is changed to $\mu = (1 - \frac{\Phi}{\Phi_m})^{-2.5}$ where Φ_m is a constant depending on the maximum packing of the imposed particles, and causes the fluid to behave as the solid. The constant Φ_m is dependent on the pattern of the packing, and very dependent on the shape of the particles introduced [26]. Krieger & Dougherty (1959) [24] extend this,

$$\mu = (1 - \frac{\Phi}{\Phi_m})^{-B\Phi_m}. \quad (2.1)$$

Now this matches the Einstein model to linear order, is valid at larger packing density and notices the importance of packing density. Although the above model captures the essential properties of the theory, it is observed in the literature that dropping the notion of packing density and the Einstein constant agrees best with the experimental data; instead treat the constants B, Φ_m as variable parameters.

3. Phase-change Boussinesq models

3.1. Main assumptions and model equations

Let $t \in (0, t_f]$ denote time and let us consider an homogeneous and isotropic porous structure occupying a spatial domain $\Omega \subset \mathbb{R}^d$, $d = 2, 3$ and saturated with an incompressible viscous fluid. This fluid has kinematic viscosity ν , thermal expansion coefficient α , and nondimensional specific heat C .

The model problem arises from the description of flow using Navier-Stokes and Stefan problems. Applying the so-called Obereck-Boussinesq approximation, one ends up with the following set of governing equations written in terms of the the velocity $\mathbf{u}(t) : \Omega \rightarrow \mathbb{R}^d$, the pressure $p(t) : \Omega \rightarrow \mathbb{R}$, and the temperature $\theta(t) : \Omega \rightarrow \mathbb{R}$:

$$\partial_t \mathbf{u} + \mathbf{u} \cdot \nabla \mathbf{u} - \frac{1}{\text{Re}} \text{div} [2\mu(\theta) \boldsymbol{\varepsilon}(\mathbf{u})] + \nabla p + \eta(\theta) \mathbf{u} = f(\theta) \mathbf{k}, \quad (3.1)$$

$$\text{div} \mathbf{u} = 0 \quad \text{in } \Omega \times (0, t_f], \quad (3.2)$$

$$\partial_t \theta + \mathbf{u} \cdot \nabla \theta - \frac{1}{C\text{Pr}} \text{div} (\kappa \nabla \theta) + \partial_t s + \mathbf{u} \cdot \nabla s = 0, \quad (3.3)$$

and which state the conservation of momentum, mass, and energy with enthalpy, respectively. In (3.1)-(3.3), $\boldsymbol{\varepsilon}(\mathbf{u}) = \frac{1}{2}(\nabla \mathbf{u} + \nabla \mathbf{u}^T)$ is the strain rate tensor, the function s is the enthalpy, the symbol \mathbf{k} stands for the unit vector pointing in the opposite direction to gravity, η, μ are nonlinear functions of temperature that encode the permeability of the porous material and the viscosity of the fluid, respectively. These functions will assume different specifications depending on the phase change model, to be discussed later on. We also define the Reynolds number $\text{Re} = \rho_{\text{ref}} V_{\text{ref}} L_{\text{ref}} \mu^{-1}$, the adimensional buoyancy force $f(\theta) = \text{Ra} \theta (\text{Pr} \text{Re}^2)^{-1}$ (depending linearly on the temperature distribution as in the classical Boussinesq approximation [9]), κ is the nondimensional heat conductivity tensor (here assumed isotropic), $\text{Ra} = g \beta L_{\text{ref}} (\theta_h - \theta_c) [\nu \alpha]^{-1}$ is the Rayleigh number, g is the gravity magnitude, $L_{\text{ref}}, \rho_{\text{ref}}, V_{\text{ref}}$ are the reference length, density, and velocity defining the flow, θ_h, θ_c are maximum and minimum temperatures, and $\text{Pr} = \nu \alpha^{-1}$ is the Prandtl number.

Boundary and initial data. Equations (3.1)-(3.3) are supplemented with boundary conditions as follows. No-slip boundary conditions are prescribed on the velocity over the whole $\partial\Omega$, and therefore an additional condition is required for pressure uniqueness; as usual we impose a zero-mean property. Regarding the energy equation, we assume that the domain boundary admits a splitting between

two disjoint sets Γ_D^θ and Γ_N^θ , where temperature and normal heat fluxes are prescribed, respectively. The system is supposed to be initially at rest and isothermal, and so we set $\mathbf{u}(0) = \mathbf{0}$, $p(0) = 0$ and $\theta(0) = \theta_0$ with θ_0 constant.

3.2. Enthalpy-Porosity models for phase change

The permeability function η appearing in the drag term is usually defined in such a way that (3.1) behaves as the well-known Carman-Kozeny equations (see e.g. the review [29]). We refer the reader to the classic papers [10][23] for those unfamiliar with the Carman-Kozeny equation. ϕ is the porosity (liquid fraction) and we define it below as a function of temperature to incorporate a phase change field.

$$\eta(\phi) = \xi \frac{(1 - \phi)^2}{\phi^3 + m}, \quad \text{with} \quad \phi = \frac{1}{2} \left[\tanh \left(\frac{5}{\delta\theta} (\theta - \theta_f) \right) + 1 \right]. \quad (3.4)$$

where $m > 0$ is a small parameter that prevents division by zero. The term $\delta\theta$ represents the temperature range corresponding to the width of the mushy region, and θ_f is a constant the jump function is regularised about and it corresponds to the melting point subject to appropriate scaling (in the sense that in the fluid one has $\phi = 1$ by setting $\eta = 0$, and in the solid $\phi = 0$ corresponds to $\eta = \xi[m]^{-1}$). This also implies that in the solid region one imposes a low permeability field that generates a large drag force. The parameter ξ is a large constant that represents the morphology of the melt front. It is related to the imposed permeability through $\xi = \frac{180}{\rho_{\text{ref}} d_m^2}$ where d_m is the particle diameter, and the constant 180 depends on the material under consideration [6]. Alternatively to (3.4), in our examples we will include a regularised jump function that takes the form

$$\eta = \frac{\eta_s}{2} [\tanh(M_\eta(\theta_f - \theta)) + 1], \quad (3.5)$$

where η_s corresponds to the relative size of the imposed force and M_η is the size of the mushy region. These constants determine the degree of regularisation of the jump. As above, in the liquid phase we have $\eta = 0$, and in the solid $\eta = \eta_s$, with η_s a large constant accounting for the morphology of the melt front.

In many models from the literature, the phase change is often described by combining the permeability (or porosity) regularised jumps with an enthalpy formulation [6]. The non-dimensional enthalpy function s should ideally be a Heaviside function assuming the values s_s in the solid, and s_l in the liquid. After regularisation using the phase change field ϕ we employ

$$s(\theta) = s_s + (s_l - s_s)\phi(\theta). \quad (3.6)$$

We will adopt this form in all of our models for phase change, so that the mushy region for the enthalpy will be predetermined by the temperature range $\Delta\theta$.

3.3. Enthalpy-Viscosity model for phase change

The incorporation of phase change can be alternatively embedded in the form of a temperature-dependent viscosity combined with an enthalpy formulation (as in e.g. [14]), hence we will be using the enthalpy equation defined previously (3.6) throughout the viscosity formulation.

We first present a model chosen from section 2. Firstly we draw a relationship between our phase function ϕ and the function Φ that represents the ratio of volume occupied by the particles; we have a natural equivalence that $\Phi = \Phi_m(1 - \phi)$ so now our ϕ corresponds to the ratio of the volume that isn't a particle, i.e the part that is permeable in a permeable field. We do this to embed the phase change and have the ratio of solid particles to liquid, dependent on the temperature (where the ratio is scaled by the maximum density packing of the solids). So as we melt a phase change material, there are less solid particles suspended in the liquid, this decreases the viscosity as is appropriate.

Rewriting the equation in terms of ϕ we have $\mu = \phi^{-B\Phi_m}$ as a model. We now only have one degree of freedom regarding the choice of the parameters, so we define $n = B\Phi_m$, to emphasise an abandonment of the concepts of packing density and Einstein coefficients, for a functional form of the equation. To avoid division by zero in the numerics we introduce a security parameter m , inspired to mimic the way the Carman-Kozeny equation has been regularised.

$$\mu = \frac{1}{\phi^n + m}. \quad (3.7)$$

Then we have that for the choice $n = 2.5$, we recover a Brinkman form but used for the phase change, but we could choose any value dependent on experimental data.

In analogy to (3.5) we will also employ

$$\mu(\theta) = \mu_l + \frac{(\mu_s - \mu_l)}{2} [\tanh(M_\mu(\theta_f - \theta)) + 1], \quad (3.8)$$

so that in the solid we have $\mu = \mu_s$, and in the liquid $\mu = \mu_l$. Here the constant M_μ encodes the width of the mushy region.

3.4. Weak formulation

Firstly let us recall some recurrent notation. For instance, we will write $L^2(\Omega)$ to denote the space of square integrable functions, and will use $H^1(\Omega)$, $\mathbf{H}^1(\Omega)$ to refer to the scalar and vector-valued Sobolev spaces $W^{1,2}(\Omega)$ and $\mathbf{W}^{1,2}(\Omega)$, respectively; whose norms will be denoted as $\|\cdot\|_{1,\Omega}$. The inner product in $L^2(\Omega)$ (or in its vectorial and tensorial counterparts) will be simply denoted as (\cdot, \cdot) and its associated norm as $\|\cdot\|$, or more explicitly as $\|\cdot\|_{0,\Omega}$. For readers who have not seen the definitions of the norms and seminorms of Sobolev spaces they are defined in the paper [2], this paper also states some standard Sobolev embeddings used in the proof of uniqueness. In addition, the space $L_0^2(\Omega)$ denotes the restriction of $L^2(\Omega)$ to functions with zero mean value over Ω . In view of incorporating the boundary conditions for velocity and temperature, we also introduce the space $\mathbf{H}_0^1(\Omega)$ of vector functions in $\mathbf{H}^1(\Omega)$ whose trace vanishes on $\partial\Omega$, and the space $H_D^1(\Omega)$ of scalar functions in $H^1(\Omega)$ whose trace vanishes on the sub-boundary Γ_D^θ .

Associated to the spaces introduced above, the following nonlinear, bilinear and trilinear forms are defined for all $\mathbf{u}, \mathbf{v}, \mathbf{w} \in \mathbf{H}^1(\Omega)$, $p, q \in L^2(\Omega)$, and $\theta, \psi \in H^1(\Omega)$

$$\begin{aligned} a_1^\theta(\mathbf{u}, \mathbf{v}) &:= \frac{2}{\text{Re}} \int_\Omega \mu(\theta) \boldsymbol{\varepsilon}(\mathbf{u}) : \boldsymbol{\varepsilon}(\mathbf{v}), \quad b(\mathbf{v}, q) := - \int_\Omega q \operatorname{div} \mathbf{v}, \quad c_1(\mathbf{w}; \mathbf{u}, \mathbf{v}) := \int_\Omega [(\mathbf{w} \cdot \nabla) \mathbf{u}] \cdot \mathbf{v}, \\ a_3(\theta, \psi) &:= \frac{1}{C_{\text{Pr}}} \int_\Omega \kappa \nabla \theta \cdot \nabla \psi, \quad c_3(\mathbf{w}; \theta, \psi) := \int_\Omega [\mathbf{w} \cdot \nabla \theta] \psi. \end{aligned} \quad (3.9)$$

On account of these definitions, we proceed to test (3.1)-(3.2) against adequate functions and integrate by parts conveniently in order to arrive at the following problem in weak form. For all $t \in (0, t_f]$, find $(\mathbf{u}, p, \theta) \in \mathbf{H}_0^1(\Omega) \times L_0^2(\Omega) \times H_D^1(\Omega)$ such that

$$\begin{aligned} (\partial_t \mathbf{u}, \mathbf{v}) + c_1(\mathbf{u}; \mathbf{u}, \mathbf{v}) + a_1^\theta(\mathbf{u}, \mathbf{v}) + (\eta(\theta) \mathbf{u}, \mathbf{v}) + b(\mathbf{v}, p) &= (f(\theta) \mathbf{k}, \mathbf{v}) \quad \forall \mathbf{v} \in \mathbf{H}_0^1(\Omega), \\ b(\mathbf{u}, q) &= 0 \quad \forall q \in L^2(\Omega), \\ (\partial_t [\theta + s], \psi) + c_3(\mathbf{u}; \theta + s, \psi) + a_3(\theta, \psi) &= 0 \quad \forall \psi \in H_D^1(\Omega). \end{aligned} \quad (3.10)$$

The forms defined in (3.9) enjoy the following properties, established in e.g. [8]

$$|a_1^\theta(\mathbf{u}, \mathbf{v})| \leq C \|\mathbf{u}\|_{1,\Omega} \|\mathbf{v}\|_{1,\Omega}, \quad |a_1^\theta(\mathbf{v}, \mathbf{v})| \geq C \|\mathbf{v}\|_{1,\Omega}^2, \quad (3.11)$$

$$|a_3(\theta, \psi)| \leq C \|\theta\|_{1,\Omega} \|\psi\|_{1,\Omega}, \quad |a_3(\psi, \psi)| \geq C \|\psi\|_{1,\Omega}^2, \quad b(\mathbf{v}, q) \leq \|\mathbf{v}\|_{1,\Omega} \|q\|, \quad (3.12)$$

$$|c_1(\mathbf{w}; \mathbf{u}, \mathbf{v})| \leq C \|\mathbf{w}\|_{1,\Omega} \|\mathbf{u}\|_{1,\Omega} \|\mathbf{v}\|_{1,\Omega}, \quad |c_3(\mathbf{w}; \theta, \psi)| \leq C \|\mathbf{w}\|_{1,\Omega} \|\theta\|_{1,\Omega} \|\psi\|_{1,\Omega}, \quad (3.13)$$

for all $\mathbf{u}, \mathbf{v}, \mathbf{w} \in \mathbf{H}_0^1(\Omega)$, $p, q \in L^2(\Omega)$, and $\theta, \psi \in H_D^1(\Omega)$. Also, there exists $C > 0$ depending only on the domain, such that

$$\sup_{\mathbf{v} \in \mathbf{H}^1(\Omega) \setminus \mathbf{0}} \frac{b(\mathbf{v}, q)}{\|\mathbf{v}\|_{1,\Omega}} \geq C\|q\| \quad \forall q \in L^2(\Omega). \quad (3.14)$$

3.5. Stability analysis

Let us rewrite the convective and advective terms using skew-symmetric weak forms as follows

$$c_1(\mathbf{w}; \mathbf{u}, \mathbf{v}) = \frac{1}{2} \int_{\Omega} [(\mathbf{w} \cdot \nabla) \mathbf{u}] \cdot \mathbf{v} - \frac{1}{2} \int_{\Omega} [(\mathbf{w} \cdot \nabla) \mathbf{v}] \cdot \mathbf{u}, \quad c_3(\mathbf{w}; \theta, \psi) = \frac{1}{2} \int_{\Omega} [\mathbf{w} \cdot \nabla \theta] \psi - \frac{1}{2} \int_{\Omega} [\mathbf{w} \cdot \nabla \psi] \theta. \quad (3.15)$$

We can now define the kernel of the bilinear form $b(\cdot, \cdot)$, characterised by the space of divergence-free velocities

$$V = \{\mathbf{v} \in \mathbf{H}_0^1(\Omega) : b(q, \mathbf{v}) = 0, \forall q \in L^2(\Omega)\}.$$

Then the incompressibility condition is included in the functional space and the pressure can be removed from the formulation.

Without enthalpy. Let us consider an enthalpy-free counterpart of (3.10) with a constant η , and proceed to derive energy estimates. This result has direct implication to the enthalpy viscosity model. Testing the energy equation against the temperature solution, and using (3.15) we obtain

$$\frac{1}{2} \partial_t \|\theta\|^2 + \frac{\kappa}{\text{Pr}} \|\nabla \theta\|^2 = 0,$$

and then one can use Gronwall's lemma to assert that

$$\|\theta\|^2 + \int_0^t \frac{2\kappa}{\text{Pr}} \|\nabla \theta\|^2 ds \leq \|\theta_0\|^2.$$

Testing now the momentum equation against the velocity solution, exploiting again (3.15), and applying Cauchy-Schwarz inequality, and the equation previous we obtain

$$\partial_t \|\mathbf{u}\|^2 + \left\| \frac{2\mu(\theta)^{0.5}}{\text{Re}^{0.5}} \boldsymbol{\varepsilon}(\mathbf{u}) \right\|^2 + 2A \|\mathbf{u}\|^2 \leq A_1^2 \|\theta_0\|^2 + \|\mathbf{u}\|^2,$$

where we have also used that $|\mathbf{k}| = 1$. We can then we invoke Gronwall's lemma once again to get

$$\|\mathbf{u}\|^2 + \int_0^t \left\| \frac{2\mu(\theta)^{0.5}}{\text{Re}^{0.5}} \boldsymbol{\varepsilon}(\mathbf{u}) \right\|^2 ds \leq \exp((1 - 2A)t) (\|\mathbf{u}_0\|^2 + \int_0^t A_1^2 \|\theta_0\|^2 ds).$$

With enthalpy. We define \mathbf{V} as

$$\mathbf{V} = \{\mathbf{v} \in \mathbf{H}_0^1; \text{div } \mathbf{v} = 0 \text{ on } \Omega\}.$$

Thus, based on (3.14) and the definition of \mathbf{V} (see [17], for instance), problem (3.10) is equivalent to the following problem: For all $t \in (0, t_f]$, find $(\mathbf{u}, \theta) \in \mathbf{V} \times H_D^1$ such that

$$\begin{aligned} (\partial_t \mathbf{u}, \mathbf{v}) + c_1(\mathbf{u}; \mathbf{u}, \mathbf{v}) + a_1^\theta(\mathbf{u}, \mathbf{v}) + (\eta(\theta) \mathbf{u}, \mathbf{v}) &= (f(\theta) \mathbf{k}, \mathbf{v}) \quad \forall \mathbf{v} \in \mathbf{V}, \\ (\partial_t [\theta + s], \psi) + c_3(\mathbf{u}; \theta + s, \psi) + a_3(\theta, \psi) &= 0 \quad \forall \psi \in H_D^1(\Omega). \end{aligned} \quad (3.16)$$

For the reader unsure on how the weak forms (3.10) (3.16) are equivalent, the reference [22] proves the equivalence of the variational form of Stokes equation and the variational form of Stokes where the incompressibility condition and pressure is embedded in the space. A divergence free space and a

inf-sup condition are needed to remove the pressure p and incompressibility condition (3.10). Using (3.15), one can see that for all $\mathbf{u} \in \mathbf{V}$, $\mathbf{v} \in \mathbf{H}^1(\Omega)$, and $\vartheta, \psi \in H^1(\Omega)$, we have

$$c_1(\mathbf{u}; \mathbf{v}, \mathbf{v}) = 0, \quad c_3(\mathbf{u}; \psi, \psi) = 0, \quad c_3(\mathbf{u}; \psi, \vartheta) = -c_3(\mathbf{u}; \vartheta, \psi).$$

These identities are crucial in the formulation of stability results and proof of uniqueness. We now introduce some lemmas to show the stability and uniqueness analysis of (3.16) and hence (3.10).

Lemma 3.1. *For $d = 2$, there holds*

$$\|\mathbf{v}\|_{4,\Omega}^2 \leq 2^{1/2} \|\mathbf{v}\|_{0,\Omega} \|\mathbf{v}\|_{1,\Omega} \quad \forall \mathbf{v} \in \mathbf{H}^1(\Omega).$$

This Poincare type inequality can be found in [2].

Lemma 3.2. *There exists $c_1 > 0$ such that*

$$\|\boldsymbol{\varepsilon}(\mathbf{v})\|_{0,\Omega}^2 + \|\mathbf{v}\|_{0,\Omega}^2 \geq c_1 \|\mathbf{v}\|_{1,\Omega}^2 \quad \forall \mathbf{v} \in \mathbf{H}^1(\Omega),$$

we have c_1 dependence on Ω .

This is Korn's inequality, for a review of the classical proof by Lions [25] and a presentation of a new proof is given in the paper [11].

Lemma 3.3. *Repeated Cauchy-Schwarz to bound a trilinear form*

$$\begin{aligned} |\int (\mathbf{a}\mathbf{b})\mathbf{c}| &\leq \left(\int (\mathbf{a}\mathbf{b})^2 \int \mathbf{c}^2 \right)^{\frac{1}{2}} \\ &\leq \left(\int (\mathbf{a}^2)\mathbf{b}^2 \int \mathbf{c}^2 \right)^{\frac{1}{2}} \\ &\leq \left(\left(\int (\mathbf{a}^2)^2 \int (\mathbf{b}^2)^2 \right)^{\frac{1}{2}} \int \mathbf{c}^2 \right)^{\frac{1}{2}} \\ &\leq \int (\mathbf{a}^4)^{\frac{1}{4}} \int (\mathbf{b}^4)^{\frac{1}{4}} \int (\mathbf{c}^2)^{\frac{1}{2}} \\ &\leq \|\mathbf{a}\|_{4,\Omega} \|\mathbf{b}\|_{4,\Omega} \|\mathbf{c}\|_{0,\Omega} \end{aligned}$$

Lemma 3.4 (Gronwall). *Let λ be a non negative function and $F_i = L^1(0, t)$ and $\int_0^t F_i(s)ds$ continuous non-decreasing on $[0, t^*]$ then*

$$\partial_t \lambda(t) + F_1(t) \leq F_2(t) + F_3(t)\lambda(t)$$

implies for almost all $t \in [0, t^]$*

$$\lambda(t) + \int_0^t F_1(s)ds \leq \exp \left[\int_0^t F_3(s) \right] \left(\lambda(0) + \int_2^t F_2(s) \right).$$

We use the Gronwall's lemma similar to how it is used in [12]. This paper is of interest to the reader, as we mention double diffusive convection later in the project.

Lemma 3.5. *Young's inequality. If $a, b, p, q \in \mathbb{R}^{>0}$, such that $\frac{1}{p} + \frac{1}{q} = 1$ then*

$$ab \leq \frac{a^p}{p} + \frac{b^q}{q}.$$

Often we choose $p = q = 2$ and introduce an ϵ

$$ab \leq \frac{a^2}{2\epsilon} + \frac{b^2\epsilon}{2}$$

Lemma 3.6. *Inequality used in the proof of uniqueness*

$$\|\bar{\theta}\|_{0,\Omega}^2 \leq \|\bar{\theta} + s(\theta_1) - s(\theta_2)\|_{0,\Omega}^2 + 2(|\bar{\theta}|, |s(\theta_1) - s(\theta_2)|)$$

Proof. Consider the inequality

$$\begin{aligned} \|a\|_{0,\Omega}^2 &\leq \|a\|_{0,\Omega}^2 + \|b\|_{0,\Omega}^2 \\ &\leq \|a + b\|_{0,\Omega}^2 + 2 \int |a||b| \end{aligned}$$

Now define $a = \bar{\theta}$, $b = s(\theta_1) - s(\theta_2)$ and we are done \square

We now establish the stability analysis of problem (3.16), where we include enthalpy and have the Darcy term η dependent on temperature. We will now suppose that the functions μ, η require uniform boundedness and Lipschitz continuity: there exist positive constants $\mu_1, \mu_2, \eta_1, \eta_2, L_\mu$ and L_η , such that

$$\eta_1 \leq \eta(\psi) \leq \eta_2, \quad |\eta(\psi) - \eta(\varphi)| \leq L_\eta |\psi - \varphi| \quad \forall \psi, \varphi \in \mathbb{R}, \quad (3.17)$$

$$\mu_1 \leq \mu(\psi) \leq \mu_2, \quad |\mu(\psi) - \mu(\varphi)| \leq L_\mu |\psi - \varphi| \quad \forall \psi, \varphi \in \mathbb{R}. \quad (3.18)$$

Similar assumptions will be placed on the source function f : we suppose that there exists positive constants C_f and L_f such that

$$|f(\psi)| \leq C_f |\psi|, \quad |f(\psi) - f(\varphi)| \leq L_f |\psi - \varphi| \quad \forall \psi, \varphi \in \mathbb{R}. \quad (3.19)$$

On the other hand, we will suppose that s is of class C^1 , and there exist positive constants s_1, s_2, L_{s_1} and L_{s_2} such that

$$|s(\psi)| \leq s_1, \quad |s(\psi) - s(\varphi)| \leq L_{s_1} |\psi - \varphi|, \quad |\nabla s(\psi)| \leq s_2 |\nabla \psi|, \quad |\nabla s(\psi) - \nabla s(\varphi)| \leq L_{s_2} |\psi - \varphi|, \quad (3.20)$$

for all $\psi, \varphi \in \mathbb{R}$. Finally, we suppose that the adimensional heat conductivity tensor κ is a uniform bounded and uniformly positive definite tensor, meaning that there exist positive constants κ_0 and κ_1 such that

$$|\kappa| \leq \kappa_1, \quad \kappa \mathbf{v} \cdot \mathbf{v} \geq \kappa_0 |\mathbf{v}|^2 \quad \forall \mathbf{v} \in \mathbb{R}^n. \quad (3.21)$$

Theorem 3.7. *Assume that $\kappa_0 > \kappa_1 s_2$. Then, for any solution of (3.16) and for any $t \in (0, t_f]$, there exists a constant C depending on $c_1, \mu_1, \text{Re}, \eta_1, C_f, \kappa_0, \kappa_1, s_2, c_p, \text{CPr}, \Omega$ and t_f such that*

$$\|\mathbf{u}\|_{\mathbf{L}^2(0,t;\mathbf{H}_0^1(\Omega))} + \|\theta\|_{\mathbf{L}^2(0,t;\mathbf{H}_D^1(\Omega))} \leq C |\mathbf{k}| \left\{ \|s_0\|_{0,\Omega} + \|\theta_0\|_{0,\Omega} \right\}. \quad (3.22)$$

Proof. Let (\mathbf{u}, θ) be the solution of (3.16). Taking $\mathbf{v} = \mathbf{u}$ in the first equation of (3.16) we get

$$\int_{\Omega} \partial_t [\mathbf{u}] \cdot \mathbf{u} + c_1(\mathbf{u}, \mathbf{u}, \mathbf{u}) + \frac{2}{\text{Re}} \int_{\Omega} \mu(\theta) \varepsilon(\mathbf{u}) : \varepsilon(\mathbf{u}) + \int_{\Omega} \eta(\theta) \mathbf{u} \cdot \mathbf{u} = \int_{\Omega} f(\theta) \mathbf{k} \cdot \mathbf{u}.$$

Apply (3.17), (3.18) and (3.19) and use the Cauchy-Schwarz' inequality on the right hand side, we obtain that

$$\frac{1}{2} \frac{d}{dt} \int_{\Omega} \mathbf{u}^2 + \frac{2\mu_1}{\text{Re}} \|\varepsilon(\mathbf{u})\|_{0,\Omega}^2 + \eta_1 \|\mathbf{u}\|_{0,\Omega}^2 \leq C_f |\mathbf{k}| \|\theta\|_{0,\Omega} \|\mathbf{u}\|_{0,\Omega},$$

this in turn is equivalent to

$$\frac{1}{2} \frac{d}{dt} \|\mathbf{u}\|_{0,\Omega}^2 + \frac{2\mu_1}{\text{Re}} \|\varepsilon(\mathbf{u})\|_{0,\Omega}^2 + \eta_1 \|\mathbf{u}\|_{0,\Omega}^2 \leq C_f |\mathbf{k}| \|\theta\|_{0,\Omega} \|\mathbf{u}\|_{0,\Omega}.$$

Next, applying Young's inequality with constant $\varepsilon = \eta_1$, with $a = C_f |\mathbf{k}| \|\theta\|_{0,\Omega}$ and $b = \|\mathbf{u}\|_{0,\Omega}$

$$\frac{1}{2} \frac{d}{dt} \|\mathbf{u}\|_{0,\Omega}^2 + \frac{2\mu_1}{\text{Re}} \|\varepsilon(\mathbf{u})\|_{0,\Omega}^2 + \frac{\eta_1}{2} \|\mathbf{u}\|_{0,\Omega}^2 \leq \frac{C_f^2 |\mathbf{k}|^2}{2\eta_1} \|\theta\|_{0,\Omega}^2.$$

We have that

$$\frac{1}{2} \frac{d}{dt} \|\mathbf{u}\|_{0,\Omega}^2 + \min \left\{ \frac{2\mu_1}{\text{Re}}, \frac{\eta_1}{2} \right\} \left(\|\varepsilon(\mathbf{u})\|_{0,\Omega}^2 + \|\mathbf{u}\|_{0,\Omega}^2 \right) \leq \frac{C_f^2 |\mathbf{k}|^2}{2\eta_1} \|\theta\|_{0,\Omega}^2,$$

By using Korn's inequality, lemma 3.2, we deduce that

$$\frac{1}{2} \frac{d}{dt} \|\mathbf{u}\|_{0,\Omega}^2 + \alpha_1 \|\mathbf{u}\|_{1,\Omega}^2 \leq \frac{C_f^2 |\mathbf{k}|^2}{2\eta_1} \|\theta\|_{0,\Omega}^2,$$

then we have upon integration between 0 and t

$$\|\mathbf{u}\|_{0,\Omega}^2 + \|\mathbf{u}\|_{\mathbf{L}^2(0,t;\mathbf{H}_0^1(\Omega))}^2 \leq C_1 |\mathbf{k}|^2 \|\theta\|_{\mathbf{L}^2(0,t;\mathbf{H}_D^1(\Omega))}^2, \quad (3.23)$$

where C_1 is a constant depending on $C_f, c_1, \mu_1, \eta_1, \text{Re}, \Omega$ and t_f .

We now try for a similar condition in temperature. Similarly to before, we take $\psi = \theta + s$ in the third row of (3.10),

$$(\partial_t[\theta + s], \theta + s) + c_3(\mathbf{u}; \theta + s, \theta + s) + a_3(\theta, \theta + s) = 0.$$

So that the c_3 term vanishes.

We split the a_3 term and and apply (3.20) and (3.21) to obtain

$$\frac{1}{2} \frac{d}{dt} \|\theta + s\|_{0,\Omega}^2 + \frac{\kappa_0}{\text{CPr}} |\theta|_{1,\Omega}^2 \leq \frac{\kappa_1 s_2}{\text{CPr}} |\theta|_{1,\Omega}^2.$$

Now, we integrate between 0 and t to obtain

$$\|\theta + s\|_{0,\Omega}^2 + \|\theta\|_{\mathbf{L}^2(0,t;\mathbf{H}_D^1(\Omega))}^2 \leq C_2 \left\{ \|s_0\|_{0,\Omega}^2 + \|\theta_0\|_{0,\Omega}^2 \right\}, \quad (3.24)$$

where $s_0 := s(\theta_0)$ and C_2 is a constant depending on $c_p, \text{CPr}, \kappa_0, \kappa_1, s_2, \Omega$ and t_f . Finally, we derive the result (3.22) from (3.23) and (3.24). □

Theorem 3.8. Assume that the data $\theta_0 \in \mathbf{L}^2(\Omega)$. Then, problem (3.10) has a solution $(\mathbf{u}, p, \theta) \in \mathbf{L}^2(0, t_f; \mathbf{H}_0^1(\Omega)) \times \mathbf{L}^2(0, t_f; \mathbf{L}_0^2(\Omega)) \times \mathbf{L}^2(0, t_f; \mathbf{H}_D^1(\Omega))$.

Proof. It follows analogously to the proof of [Theorem 2.3][1] by applying the assumptions (3.17)-(3.20). Basically, it is a consequence of density arguments, the Cauchy-Lipschitz theorem and the inf-sup condition. □

The following result establishes the uniqueness of problem (3.10) and is found in [3].

Theorem 3.9. *Let $d = 2$. If the problem (3.10) admits a solution $(\mathbf{u}, \theta, p) \in \mathbf{L}^p(0, t_f; \mathbf{W}^{1,r}(\Omega)) \times \mathbf{L}^2(0, t_f; \mathbf{H}_0^1(\Omega)) \times \mathbf{L}^2(0, t_f; \mathbf{L}_0^2(\Omega))$, with $p \geq 4$ and $r \geq 4$, and $L_{s_1} < 1/2$, then this solution is unique.*

Proof. Let $(\mathbf{u}_1, p_1, \theta_1)$ and $(\mathbf{u}_2, p_2, \theta_2)$ be two solutions of (3.10). With the aim to prove uniqueness, we denote $\bar{\mathbf{u}} = \mathbf{u}_1 - \mathbf{u}_2$, $\bar{p} = p_1 - p_2$ and $\bar{\theta} = \theta_1 - \theta_2$. Now, from the third equation in (3.10), by adding and subtracting $c_3(\mathbf{u}_2, \theta_1 + s(\theta_1), \psi)$, with $\psi = \bar{\theta} + s(\theta_1) - s(\theta_2)$, applying Cauchy-Schwarz inequality, and using lemma 3.3 we obtain that

$$\begin{aligned} & \frac{1}{2} \frac{d}{dt} \|\bar{\theta} + s(\theta_1) - s(\theta_2)\|_{0,\Omega}^2 + \frac{1}{\text{CPr}} \kappa_0 |\bar{\theta}|_{1,\Omega}^2 \\ & \leq \frac{\kappa_1 L_{s_2}}{\text{CPr}} |\bar{\theta}|_{1,\Omega} \|\bar{\theta}\|_{0,\Omega} + |\theta_1 + s(\theta_1)|_{1,\Omega} \|\bar{\mathbf{u}}\|_{4,\Omega} \|\bar{\theta} + s(\theta_1) - s(\theta_2)\|_{4,\Omega}. \end{aligned}$$

For the reader not used to this type of proof, the first line is derived in the appendix. Next, using Young's inequality to the right hand side terms with constants $\varepsilon_3, 1$ respectively. Followed by lemma 3.1 shortly afterwards, we deduce that

$$\begin{aligned} & \frac{1}{2} \frac{d}{dt} \|\bar{\theta} + s(\theta_1) - s(\theta_2)\|_{0,\Omega}^2 + \frac{1}{\text{CPr}} \kappa_0 |\bar{\theta}|_{1,\Omega}^2 \\ & \leq \frac{\kappa_1 L_{s_2}}{\text{CPr}} \left\{ \frac{1}{2\varepsilon_3} |\bar{\theta}|_{1,\Omega}^2 + \frac{\varepsilon_3}{2} \|\bar{\theta}\|_{0,\Omega}^2 \right\} + \frac{1}{\sqrt{2}} |\theta_1 + s(\theta_1)|_{1,\Omega} \|\bar{\mathbf{u}}\|_{0,\Omega} \|\bar{\mathbf{u}}\|_{1,\Omega} \\ & \quad + \frac{1}{\sqrt{2}} |\bar{\theta} + s(\theta_1) - s(\theta_2)|_{1,\Omega} \|\bar{\theta} + s(\theta_1) - s(\theta_2)\|_{0,\Omega} |\theta_1 + s(\theta_1)|_{1,\Omega}. \end{aligned}$$

Finally, by applying again Young's inequality to the last two terms on the right hand side with constants ε_4 and ε_5 respectively. And also using the identity $(a + b)^2 \leq 2(a^2 + b^2)$ we get

$$\begin{aligned} & \frac{1}{2} \frac{d}{dt} \|\bar{\theta} + s(\theta_1) - s(\theta_2)\|_{0,\Omega}^2 + \frac{1}{\text{CPr}} \kappa_0 |\bar{\theta}|_{1,\Omega}^2 \\ & \leq \frac{\kappa_1 L_{s_2}}{\text{CPr}} \left\{ \frac{1}{2\varepsilon_3} |\bar{\theta}|_{1,\Omega}^2 + \frac{\varepsilon_3}{2} \|\bar{\theta}\|_{0,\Omega}^2 \right\} + \frac{1}{\sqrt{2}} \left\{ \frac{1}{2} \varepsilon_4 |\bar{\mathbf{u}}|_{1,\Omega}^2 + \frac{1}{2\varepsilon_4} |\theta_1 + s(\theta_1)|_{1,\Omega}^2 \|\bar{\mathbf{u}}\|_{0,\Omega}^2 \right\} \\ & \quad + \frac{1}{\sqrt{2}} \left\{ \varepsilon_5 (\|\bar{\theta}\|_{1,\Omega}^2 + L_{s_2}^2 \|\bar{\theta}\|_{0,\Omega}^2) + \frac{(L_{s_1}^2 + 1)}{\varepsilon_5} \|\bar{\theta}\|_{0,\Omega}^2 |\theta_1 + s(\theta_1)|_{1,\Omega}^2 \right\}. \end{aligned} \quad (3.25)$$

Analogously, from the first equation in (3.10), adding and subtracting the terms $c_1(\mathbf{u}_2, \mathbf{u}_1, \mathbf{v})$, $(\eta(\theta_2)\mathbf{u}_1, \mathbf{v})$ and $\frac{2}{\text{Re}}(\mu(\theta_2)\varepsilon(\mathbf{u}_1), \varepsilon(\mathbf{v}))$, with $\mathbf{v} = \bar{\mathbf{u}}$, applying Cauchy-Schwarz inequality lemma 3.3, and the Lipschitz continuity of f 3.19 we find that

$$\begin{aligned} & \frac{1}{2} \frac{d}{dt} \|\bar{\mathbf{u}}\|_{0,\Omega}^2 + \frac{2\mu_1}{\text{Re}} \|\varepsilon(\bar{\mathbf{u}})\|_{0,\Omega}^2 + \eta_1 \|\bar{\mathbf{u}}\|_{0,\Omega}^2 \\ & \leq \|\bar{\mathbf{u}}\|_{4,\Omega}^2 \|\bar{\mathbf{u}}\|_{1,\Omega} + \frac{2}{\text{Re}} |((\mu(\theta_1) - \mu(\theta_2))\varepsilon(\mathbf{u}_1), \varepsilon(\bar{\mathbf{u}}))| + L_\eta \|\mathbf{u}_1\|_{0,\Omega} \|\bar{\theta}\|_{4,\Omega} \|\bar{\mathbf{u}}\|_{4,\Omega} + L_f |\mathbf{k}| \|\bar{\theta}\|_{0,\Omega} \|\bar{\mathbf{u}}\|_{0,\Omega}. \end{aligned} \quad (3.26)$$

Thus, on the left hand side of (3.26), we apply Korn's inequality, using the trick to absorb the constant seen in the stability argument. While on the right hand side, for the first, third and fourth term, we apply Young's inequality with constants $\varepsilon_6, \varepsilon_7$ and ε_8 to obtain

$$\begin{aligned} & \frac{1}{2} \frac{d}{dt} \|\bar{\mathbf{u}}\|_{0,\Omega}^2 + \alpha_3 \|\bar{\mathbf{u}}\|_{1,\Omega}^2 \\ & \leq \frac{1}{2} \varepsilon_6 |\bar{\mathbf{u}}|_{1,\Omega}^2 + \frac{1}{2\varepsilon_6} \|\bar{\mathbf{u}}\|_{0,\Omega}^2 |\mathbf{u}_1|_{1,\Omega}^2 + \frac{2}{\text{Re}} |((\mu(\theta_1) - \mu(\theta_2))\varepsilon(\mathbf{u}_1), \varepsilon(\bar{\mathbf{u}}))| \\ & \quad + \frac{1}{\sqrt{2}} L_\eta \|\mathbf{u}_1\|_{0,\Omega} \left\{ \frac{1}{2} \varepsilon_7 \|\bar{\theta}\|_{0,\Omega}^2 + \frac{1}{2\varepsilon_7} |\bar{\theta}|_{1,\Omega}^2 \right\} + \frac{1}{\sqrt{2}} L_\eta \|\mathbf{u}_1\|_{0,\Omega} \left\{ \frac{1}{2\varepsilon_8} |\bar{\mathbf{u}}|_{1,\Omega}^2 + \frac{1}{2} \varepsilon_8 \|\bar{\mathbf{u}}\|_{0,\Omega}^2 \right\} \\ & \quad + \frac{1}{2} L_f |\mathbf{k}| \{ \|\bar{\theta}\|_{0,\Omega}^2 + \|\bar{\mathbf{u}}\|_{0,\Omega}^2 \}, \end{aligned} \quad (3.27)$$

where $\alpha_3 := c_1 \min \left\{ \frac{2\mu_1}{\text{Re}}, \eta_1 \right\}$, we have also made use of 3.17, lemma 3.3 as well as Young's inequality again.

Now, since the exact solution $\mathbf{u}_1 \in \mathbf{L}^p(0, t_f, \mathbf{W}^{1,r}(\Omega))$, $r \geq 4$, $p \geq 4$, using Hölder's and Young's inequalities with constants r , $r^* := \frac{2r}{r-2}$ and ε_9 , ε_{10} , respectively, to the last term of (3.27), and use of standard Sobolev embedding theorems, see lemma 2.1 in the paper [15]. We deduce that

$$\begin{aligned} \frac{2}{\text{Re}} |((\mu(\theta_1) - \mu(\theta_2))\varepsilon(\mathbf{u}_1) : \varepsilon(\bar{\mathbf{u}}))| &\leq \frac{2L_\mu}{\text{Re}} \left\{ \frac{\varepsilon_9}{2} \|\mathbf{u}_1\|_{1,r,\Omega} \|\bar{\mathbf{u}}\|_{1,\Omega}^2 + \frac{1}{2\varepsilon_9} \|\mathbf{u}_1\|_{1,r,\Omega} \|\bar{\theta}\|_{r^*,\Omega}^2 \right\} \\ &\leq \frac{L_\mu \varepsilon_9}{\text{Re}} \|\mathbf{u}_1\|_{1,r,\Omega} \|\bar{\mathbf{u}}\|_{1,\Omega}^2 + \frac{L_\mu}{\varepsilon_9 \text{Re}} \|\mathbf{u}_1\|_{1,r,\Omega} \left\{ \frac{1}{\sqrt{2}\varepsilon_{10}} \|\bar{\theta}\|_{0,\Omega}^2 + \frac{\varepsilon_{10}}{\sqrt{2}} \|\bar{\theta}\|_{1,\Omega}^2 \right\}. \end{aligned} \quad (3.28)$$

We add together (3.25) and (3.27) making use of (3.28). We then try and remove the terms with no time derivative on the left hand side by appropriate choice of parameters. For example choosing $\varepsilon_3 = \frac{2\kappa_1 L_{s_2}}{\kappa_0}$, $\varepsilon_4 = \frac{\alpha_3}{\sqrt{2}}$, $\varepsilon_5 = \frac{\kappa_0}{2\sqrt{2}\text{CPr}}$, $\varepsilon_6 = \frac{\alpha_3}{2}$, $\varepsilon_7 = \frac{\sqrt{2}\text{CPr}L_\eta \|\mathbf{u}_1\|_{0,\Omega}}{\kappa_0}$, $\varepsilon_8 = \frac{\sqrt{2}L_\eta \|\mathbf{u}_1\|_{0,\Omega}}{\alpha_3}$, $\varepsilon_9 = \frac{\alpha_3 \text{Re}}{4L_\mu \|\mathbf{u}_1\|_{1,r,\Omega}}$ and $\varepsilon_{10} = \frac{\kappa_0 \varepsilon_9 \text{Re}}{2\sqrt{2}\text{CPr}L_\mu \|\mathbf{u}_1\|_{1,r,\Omega}}$ we obtain that

$$\begin{aligned} \frac{1}{2} \frac{d}{dt} (\|\bar{\theta} + s(\theta_1) - s(\theta_2)\|_{0,\Omega}^2 + \|\bar{\mathbf{u}}\|_{0,\Omega}^2) \\ \leq \tilde{C} (\|\theta_1 + s(\theta_1)\|_{1,\Omega}^2 + \|\mathbf{u}_1\|_{1,r,\Omega}^4 + \|\mathbf{u}_1\|_{0,\Omega}^2 + 1) (\|\bar{\mathbf{u}}\|_{0,\Omega}^2 + \|\bar{\theta}\|_{0,\Omega}^2). \end{aligned}$$

Integrating between 0 and t on the last inequality, and then, adding on both sides the term $2(|\theta|, |s(\theta_1) - s(\theta_2)|)$, We then employ the lemma 3.5 to remove the enthalpy from the left hand side. We use 3.20 on the term on the right hand side. We then use the assumption given in the theorem statement $L_{s_1} \leq 1/2$, we get

$$\|\bar{\theta}\|_{0,\Omega}^2 + \|\bar{\mathbf{u}}\|_{0,\Omega}^2 \leq \hat{C} \int_0^t (\|\theta_1 + s(\theta_1)\|_{1,\Omega}^2 + \|\mathbf{u}_1\|_{1,r,\Omega}^4 + \|\mathbf{u}_1\|_{0,\Omega}^2 + 1) (\|\bar{\mathbf{u}}\|_{0,\Omega}^2 + \|\bar{\theta}\|_{0,\Omega}^2) dt.$$

Finally, by applying Gronwall's lemma, we obtain $\bar{\mathbf{u}} = \mathbf{0}$ and $\bar{\theta} = 0$. Moreover, from the relation

$$(\text{div } \mathbf{v}, \bar{p}) = 0 \quad \forall \mathbf{v} \in \mathbf{H}_0^1(\Omega)$$

we deduce $\bar{p} = 0$, concluding the proof. \square

The above proof will be found in [3], but the steps are expanded upon in the presentation above to make it more accessible. The difficult inequality (3.28), is given in more detail in the preprint [15], including the exact Sobolev embeddings used. The proof is used to deal with nonlinear viscosity of the Boussinesq problem, our proof is different in the fact that we have more terms like enthalpy and porosity. The the porosity is dealt with almost entirely by lemma 3.2 it is the enthalpy terms that gives more issues for the uniqueness.

We note the condition needed for the of proof uniqueness is actually quite restrictive; $L_{s_1} \leq 1/2$ doesn't hold for the enthalpy jump function used in the numerical phase change model. We might still have a unique solution, but this proof doesn't apply.

4. Finite element scheme

Let $\{\mathcal{T}_h\}_{h>0}$ be a shape-regular family of partitions of the region $\bar{\Omega}$, by triangles (or tetrahedrons in 3D) K of diameter h_K , with overall meshsize $h := \max\{h_K : K \in \mathcal{T}_h\}$. In what follows, given an integer $k \geq 1$ and a subset S of \mathbb{R}^d , $\mathbb{P}_k(S)$ will denote the space of polynomial functions defined locally in S and being of total degree $\leq k$.

4.1. A finite element method

The spatial discretisation will be based on the finite element method. Accordingly, we define the following finite-dimensional spaces for the approximation of velocity, pressure, and temperature respectively:

$$\begin{aligned} \mathbf{V}_h &:= \{\mathbf{v}_h \in \mathbf{H}^1(\Omega) : \mathbf{v}_h|_K \in [\mathbb{P}_{k+1}(K)]^d \ \forall K \in \mathcal{T}_h, \text{ and } \mathbf{v}_h = \mathbf{0} \text{ on } \partial\Omega\}, \\ Q_h &:= \{q_h \in L^2(\Omega) : q_h|_K \in \mathbb{P}_k(K) \ \forall K \in \mathcal{T}_h, \text{ and } \int_{\Omega} q_h = 0\}, \\ Z_h &:= \{\psi_h \in H^1(\Omega) : \psi_h|_K \in \mathbb{P}_{k+1}(K) \ \forall K \in \mathcal{T}_h, \text{ and } \psi_h = 0 \text{ on } \Gamma_D^\theta\}, \end{aligned} \quad (4.1)$$

for $k \geq 1$, which satisfy the discrete inf-sup condition: There exists a constant $C^* \geq 0$ independent of h such that

$$\sup_{\mathbf{v}_h \in \mathbf{V}_h \setminus \mathbf{0}} \frac{b(\mathbf{v}_h, q_h)}{\|\mathbf{v}_h\|_{1,\Omega}} \geq C^* \|q_h\|_{0,\Omega} \quad \forall q_h \in Q_h. \quad (4.2)$$

Then the semi-discrete Galerkin method associated to (3.10) reads: For all $t \in (0, t_f]$, find $(\mathbf{u}_h, p_h, \theta_h) \in \mathbf{V}_h \times Q_h \times Z_h$ such that

$$\begin{aligned} (\partial_t \mathbf{u}_h, \mathbf{v}_h) + c_1(\mathbf{u}_h; \mathbf{u}_h, \mathbf{v}_h) + a_1^{\theta_h}(\mathbf{u}_h, \mathbf{v}_h) + (\eta(\theta_h) \mathbf{u}_h, \mathbf{v}_h) + b(\mathbf{v}_h, p_h) &= (f(\theta_h) \mathbf{k}, \mathbf{v}_h) \quad \forall \mathbf{v}_h \in \mathbf{V}_h, \\ b(\mathbf{u}_h, q_h) - \gamma(p_h, q_h) &= 0 \quad \forall q_h \in Q_h, \\ (\partial_t [\theta_h + s_h], \psi_h) + c_3(\mathbf{u}_h; \theta_h + s_h, \psi_h) + a_3(\theta_h, \psi_h) &= 0 \quad \forall \psi_h \in Z_h. \end{aligned} \quad (4.3)$$

The second term in the left hand side of the weak form for the mass conservation equation appears as a pressure penalty term that accounts for uniqueness of discrete pressure, and $\gamma > 0$ is a small constant.

So far we have a semi discrete method, we are continuous in time, but discrete in space. We have chosen the finite element spaces based on Taylor-hood elements, but other options like the mini-element spaces, would also be applicable. The key is that the velocity space is enriched as compared with the pressure space. We now turn to discretising in time.

A fully discrete method will be obtained after applying the method of lines. Regarding the time discretisation of (4.3), and in view of the overall second order space discretisation expected when choosing $k = 1$, we here employ a fully implicit second-order backward differentiation formula (BDF2, see e.g. [28]). This choice provides unconditional stability and permits to take sufficiently large timesteps to reach approximate steady state solutions, should they exist. Let $0 = t^0 < t^1 < \dots < t^N = t_f$ be a uniform partition of the time interval into equispaced subintervals of size Δt , then the method reads: For $n = 0$ apply a first order backward Euler method, starting from the initial values $\mathbf{u}_h^0, \theta_h^0$, which are taken as interpolates of the initial data \mathbf{u}^0, θ^0 , onto \mathbf{V}_h and Z_h . Below is the non-linear system we solve for $\mathbf{u}_h^1, \theta_h^1$.

$$\begin{aligned} &\frac{1}{\Delta t}(\mathbf{u}_h^{n+1}, \mathbf{v}_h) + c_1(\mathbf{u}_h^{n+1}; \mathbf{u}_h^{n+1}, \mathbf{v}_h) + a_1^{\theta_h^{n+1}}(\mathbf{u}_h^{n+1}, \mathbf{v}_h) \\ &+ (\eta(\theta_h^{n+1}) \mathbf{u}_h^{n+1}, \mathbf{v}_h) + b(\mathbf{v}_h, p_h^{n+1}) - (f(\theta_h^{n+1}) \mathbf{k}, \mathbf{v}_h) = \frac{1}{\Delta t}(\mathbf{u}_h^n, \mathbf{v}_h) \quad \forall \mathbf{v}_h \in \mathbf{V}_h, \\ &b(\mathbf{u}_h^{n+1}, q_h) = 0 \quad \forall q_h \in Q_h, \\ &\frac{1}{\Delta t}(\theta_h^{n+1} + s_h^{n+1}, \psi_h) + c_3(\mathbf{u}_h^{n+1}; \theta_h^{n+1} + s_h^{n+1}, \psi_h) \\ &+ a_3(\theta_h^{n+1}, \psi_h) = \frac{1}{\Delta t}([\theta_h^n + s_h^n], \psi_h) \quad \forall \psi_h \in Z_h, \end{aligned} \quad (4.4)$$

Then for $n = 1, 2, \dots$, we solve the non-linear system corresponding to the BDF-2 discretisation

in time.

$$\begin{aligned}
& \frac{3}{2\Delta t}(\mathbf{u}_h^{n+1}, \mathbf{v}_h) + c_1(\mathbf{u}_h^{n+1}; \mathbf{u}_h^{n+1}, \mathbf{v}_h) + a_1^{\theta_h^{n+1}}(\mathbf{u}_h^{n+1}, \mathbf{v}_h) \\
& + (\eta(\theta_h^{n+1})\mathbf{u}_h^{n+1}, \mathbf{v}_h) + b(\mathbf{v}_h, p_h^{n+1}) - (f(\theta_h^{n+1})\mathbf{k}, \mathbf{v}_h) = \frac{1}{\Delta t}(2\mathbf{u}_h^n - \frac{1}{2}\mathbf{u}_h^{n-1}, \mathbf{v}_h) \quad \forall \mathbf{v}_h \in \mathbf{V}_h, \\
& b(\mathbf{u}_h^{n+1}, q_h) = 0 \quad \forall q_h \in \mathbf{Q}_h, \quad (4.5) \\
& \frac{3}{2\Delta t}(\theta_h^{n+1} + s_h^{n+1}, \psi_h) + c_3(\mathbf{u}_h^{n+1}; \theta_h^{n+1} + s_h^{n+1}, \psi_h) \\
& + a_3(\theta_h^{n+1}, \psi_h) = \frac{1}{\Delta t}(2[\theta_h^n + s_h^n] - \frac{1}{2}[\theta_h^{n-1} + s_h^{n-1}], \psi_h) \quad \forall \psi_h \in \mathbf{Z}_h,
\end{aligned}$$

4.2. Consistent linearisation

Problem (4.5) and (4.4) entails solving a system of nonlinear equations at the timesteps $n \geq 1$, $n = 0$ respectively. For a fixed timestep the solution of this nonlinear system of equations we will employ Newton Raphson's method, which features quadratic convergence provided the initial guess is sufficiently close to the zone of attraction. For a generic nonlinear problem $\mathbf{F}(\mathbf{w}) = \mathbf{0}$, one produces a sequence $\{\mathbf{w}^k\}_k$ converging quadratically to \mathbf{w} , through the Newton iterates

$$\mathcal{D}\mathbf{F}(\mathbf{w}^k)[\delta \mathbf{w}] = -\mathbf{F}(\mathbf{w}^k) \quad \text{where} \quad \delta \mathbf{w} = \mathbf{w}^{k+1} - \mathbf{w}^k, \quad \mathbf{w}^0 = (\mathbf{u}_h^n, p_h^n, \theta_h^n),$$

where $\mathcal{D}\mathbf{F}(v)[\delta v]$ denotes the Gâteaux derivative of the functional \mathbf{F} along the direction δv . Then at each Newton step k we solve the linear problem

$$\begin{aligned}
& \frac{3}{2\Delta t}(\delta \mathbf{u}_h, \mathbf{v}_h) + c_1(\delta \mathbf{u}_h; \mathbf{u}_h^k, \mathbf{v}_h) + c_1(\mathbf{u}_h^k; \delta \mathbf{u}_h, \mathbf{v}_h) + \frac{2}{\text{Re}}(\mu'(\theta_h^k)\delta \theta_h \varepsilon(\mathbf{u}_h^k), \varepsilon(\mathbf{v}_h)) \\
& + \frac{2}{\text{Re}}(\mu(\theta_h^k)\varepsilon(\delta \mathbf{u}_h), \varepsilon(\mathbf{v}_h)) + (\eta'(\theta_h^k)\delta \theta_h \mathbf{u}_h^k, \mathbf{v}_h) + (\eta(\theta_h^k)\delta \mathbf{u}_h, \mathbf{v}_h) + b(\mathbf{v}_h, \delta p_h) - (f'(\theta_h^k)\delta \theta_h \mathbf{k}, \mathbf{v}_h) \\
& = \frac{1}{\Delta t}(2\mathbf{u}_h^n - \frac{1}{2}\mathbf{u}_h^{n-1}, \mathbf{v}_h) + (\mathcal{R}_h^1(\mathbf{u}_h^k, p_h^k, \theta_h^k), \mathbf{v}_h) \quad \forall \mathbf{v}_h \in \mathbf{V}_h, \\
& b(\delta \mathbf{u}_h, q_h) - \gamma(\delta p_h, q_h) = (\mathcal{R}_h^2(\mathbf{u}_h^k, p_h^k, \theta_h^k), q_h) \quad \forall q_h \in \mathbf{Q}_h, \\
& \frac{3}{2\Delta t}(\delta \theta_h + s'(\theta_h^k)\delta \theta_h, \psi_h) + c_3(\delta \mathbf{u}_h; \theta_h^k + s(\theta_h^k), \psi_h) + c_3(\mathbf{u}_h^k; \delta \theta_h + s'(\theta_h^k)\delta \theta_h, \psi_h) + a_3(\delta \theta_h, \psi_h) \\
& = \frac{1}{\Delta t}(2[\theta_h^n + s_h^n] - \frac{1}{2}[\theta_h^{n-1} + s_h^{n-1}], \psi_h) + (\mathcal{R}_h^3(\mathbf{u}_h^k, p_h^k, \theta_h^k), \psi_h) \quad \forall \psi_h \in \mathbf{Z}_h.
\end{aligned}$$

where the terms \mathcal{R}_h^i stand for the Newton residuals associated to the momentum, mass, and energy-enthalpy equations. Defined as

$$\begin{aligned}
(\mathcal{R}_h^1(\mathbf{u}_h^k, p_h^k, \theta_h^k), \mathbf{v}_h) &= -c_1(\mathbf{u}_h^k; \mathbf{u}_h^k, \mathbf{v}_h) - \frac{2}{\text{Re}}(\mu(\theta_h^k)\varepsilon(\mathbf{u}_h^k), \varepsilon(\mathbf{v}_h)) - (\eta(\theta_h^k)\delta \mathbf{u}_h, \mathbf{v}_h) \\
&\quad - b(\mathbf{v}_h, p_h^k) - \frac{3}{2\Delta t}(\mathbf{u}_h^k, \mathbf{v}_h), \\
(\mathcal{R}_h^2(\mathbf{u}_h^k, p_h^k, \theta_h^k), q_h) &= -b(\mathbf{u}_h^k, q_h) + \gamma(p_h^k, \mathbf{v}_h), \\
(\mathcal{R}_h^3(\mathbf{u}_h^k, p_h^k, \theta_h^k), \psi_h) &= -\frac{3}{2\Delta t}(\theta_h^k + s(\theta_h^k), \psi_h) - c_3(\mathbf{u}_h^k, \theta_h^k + s(\theta_h^k), \psi_h) - a_3(\theta_h^k, \psi_h).
\end{aligned}$$

The omission of the linear system arising from the first time step is deliberate to avoid repetition. The matrix system arising from the model is given in the appendix.

One readily notes that as we increase the Rayleigh number, the coupling between the Navier-Stokes and the temperature equation becomes stronger. This makes the radius of convergence for the Newton method smaller (see e.g. [21]). As the new initial guess in the time-dependent method is the solution at the previous timestep, this condition reflects on a restriction on the timestep, for the

implicit backward Euler method and BFD-2 method used for time discretisation. It is emphasised that this is different from the CFL condition that would be obtained from the forwards time method. We also note that the regularity of the jump function effects this time stepping restriction.

5. Numerical tests

We stress that the zero-mean condition enforcing the uniqueness of the pressure is implemented using a pressure penalisation approach[33]. All nonlinear systems undergo a Newton linearisation with fixed residual tolerance of 1E-6. In addition, the resulting linear solves are performed with the direct method SuperLU.

5.1. Experimental convergence for the semidiscrete and fully discrete methods

For our first example we produce the error history associated with the finite element approximation. Let us consider the following closed-form solutions to the stationary Boussinesq equations with enthalpy, defined on the unit square domain $\Omega = (0, 1)^2$:

$$\mathbf{u}(x, y) = \begin{pmatrix} \sin(\pi x)^2 \sin(\pi y)^2 \cos(\pi y) \\ -\frac{1}{3} \sin(2\pi x) \sin(\pi y)^3 \end{pmatrix}, \quad p(x, y) = 10(x^4 - y^4), \quad \theta(x, y) = 1 + \sin(\pi x) \cos(\pi y).$$

These functions are smooth and they are used to generate non-homogeneous forcing and source terms. The vertical walls constitute Γ_D^θ and the bottom and top lids of the domain Γ_N^θ . The temperature-dependent viscosity, porosity, buoyancy, and enthalpy functions are taken as

$$\eta(\theta) := 2 + \tanh\left(\frac{1}{2} - \theta\right), \quad \mu(\theta) := \exp(-\theta), \quad f(\theta) := \frac{\text{Ra}}{\text{Pr Re}^2} \theta, \quad s(\theta) := 1 + \tanh(1 - \theta), \quad (5.1)$$

respectively, and the remaining parameters specifying this steady-state version of (3.1)-(3.3) are $\text{Re} = 10$, $\text{Ra} = 100$, $\text{Pr} = 0.71$, $\gamma = 1\text{E-}6$. We then construct a sequence of successively refined meshes for Ω and proceed to compute errors between approximate and exact solutions, together with local convergence rates. The outcome of this error study is depicted in Table 1, which shows optimal convergence $O(h^{k+1})$ for velocity, pressure, and temperature in their natural norms.

The error associated to the time discretisation is assessed by considering the original transient problem, with enthalpy, and employing the following exact solutions (proposed in [17] for the study of the Boussinesq approximation without enthalpy), defined on the three-dimensional domain $\Omega = (0, 1)^3$:

$$\mathbf{u}(x, y, z, t) = \begin{pmatrix} x^2 + xy - z^2 + yz \\ -2xy - \frac{1}{2}y^2 + 2yz - 2xz \\ z^2 + y^2 - x^2 + 3xy \end{pmatrix} \sin(t), \quad p(x, y, z, t) = [x - y + 3z - 3/2] \sin(t),$$

$$\theta(x, y, z, t) = 2 + [x^2 + y^2 + z^2 + 1] \sin(t).$$

The regularity of these solutions imply that the spatial finite element discretisation using a method with $k = 1$ will be machine-precision accurate, and so the total error will practically coincide with the time discretisation error. The temperature-dependent functions are taken as in (5.1). We proceed to discretise the time interval into a sequence of successively refined grids and compute accumulative errors, defined for a generic field scalar or vector field v as $E(v) := [\Delta t \sum_{n=1}^N |v_h^n - v(t^n)|^2]^{1/2}$, up to the adimensional final time $t_f = 1$. The error history is displayed in Table 2, showing a second order convergence consistently with the BDF2 algorithm employed.

DoF	h	$\ \mathbf{u} - \mathbf{u}_h\ _{1,\Omega}$	rate	$\ p - p_h\ $	rate	$\ \theta - \theta_h\ _{1,\Omega}$	rate	iter
$k = 1$								
84	0.7071	4.4051	–	0.6275	–	0.3791	–	5
268	0.3536	0.8306	2.407	0.1468	2.096	0.1027	1.884	4
948	0.1768	0.1334	2.638	0.0357	2.038	0.02654	1.953	4
3556	0.0884	0.0239	2.478	0.0088	2.013	0.0067	1.983	4
13764	0.0442	0.0051	2.226	0.0022	2.004	0.0017	1.993	4
54148	0.0221	0.0012	2.074	0.0006	2.001	0.0004	1.997	5
214788	0.0110	0.0003	2.015	0.0001	1.999	0.0001	1.999	4
$k = 2$								
172	0.7071	0.8695	–	0.102	–	0.0994	–	4
588	0.3536	0.1741	2.320	0.0145	2.813	0.0130	2.931	5
2164	0.1768	0.0253	2.779	0.0019	2.873	0.0016	2.991	5
8292	0.0884	0.0034	2.907	0.0003	2.928	0.0002	3.000	5
32452	0.0442	0.0004	2.954	3.38e-5	2.949	2.56e-5	3.001	5
128388	0.0221	6.16e-5	2.824	6.36e-6	2.961	3.21e-6	2.997	5
510724	0.0110	1.43e-5	2.983	1.51e-6	2.984	8.01e-7	2.997	4

Table 1: Error history (errors on a sequence of successively refined grids, experimental convergence rates, and Newton iteration count at each refinement level) associated to the spatial discretisation using the finite element spaces (4.1) with $k = 1$ and $k = 2$.

Δt	$E(\mathbf{u})$	rate	$E(p)$	rate	$E(\theta)$	rate	avg(iter)
1	0.1355	–	1.2943	–	0.2627	–	5
0.25	0.0176	1.9388	0.1640	1.9255	0.0329	1.8904	4.2
0.0613	0.0023	1.9905	0.0251	1.9344	0.0041	1.9587	4.2
0.0151	0.0003	1.9836	0.0032	1.9620	0.0005	1.9471	4.2

Table 2: Time discretisation errors produced with a BDF2 method on different timestep resolutions, convergence rates, and average number of Newton iterations.

5.2. Benchmark test: natural convection of air

We further validate the numerical method against a well-documented benchmark, the natural convection of air in a differentially heated square cavity $\Omega = (0,1)^2$. In this problem we do not have the enthalpy terms, we do not consider the temperature-dependent drag contribution, and the viscosity and conduction coefficients are constant. Therefore the scaling of the equations is as follows

$$\begin{aligned}
\partial_t \mathbf{u} + \mathbf{u} \cdot \nabla \mathbf{u} - \text{Pr} \Delta \mathbf{u} + \nabla p + \eta(\theta) \mathbf{u} &= \text{Ra Pr} \theta \mathbf{k}, \\
\text{div } \mathbf{u} &= 0 \\
\partial_t \theta + \mathbf{u} \cdot \nabla \theta - \Delta \theta &= 0,
\end{aligned}
\quad \text{in } \Omega \times (0, t_f],$$

where $\mathbf{k} = (0,1)^T$, and the only non-dimensional parameters and their values are $\text{Ra} = 1\text{E}5$ and $\text{Pr} = 0.71$. We use a constant timestep of $\Delta t = 0.001$ and employ a rather coarse mesh with meshsize $h = \sqrt{2}/64$. The initial conditions on the domain interior are $\mathbf{u}(0) = \mathbf{0}$ and $\theta(0) = 0.5$, and we prescribe $\theta = 1$ on the left and $\theta = 0$ on the right walls of the cavity (also for the initial datum). The upper and lower plates constitute the boundary Γ_N^θ , where we set zero-flux boundary conditions for temperature (representing insulated walls); and on all four sides of the container we impose no-slip velocities $\mathbf{u} = \mathbf{0}$.

The simulation is run until the final adimensional time $t_f = 0.5$, using a Taylor-Hood finite element family for the approximation of velocity and pressure (i.e., $k = 1$), and the pressure penalty parameter takes the value $\gamma = 1\text{E}-7$. The flow is driven by the difference of temperature and examples

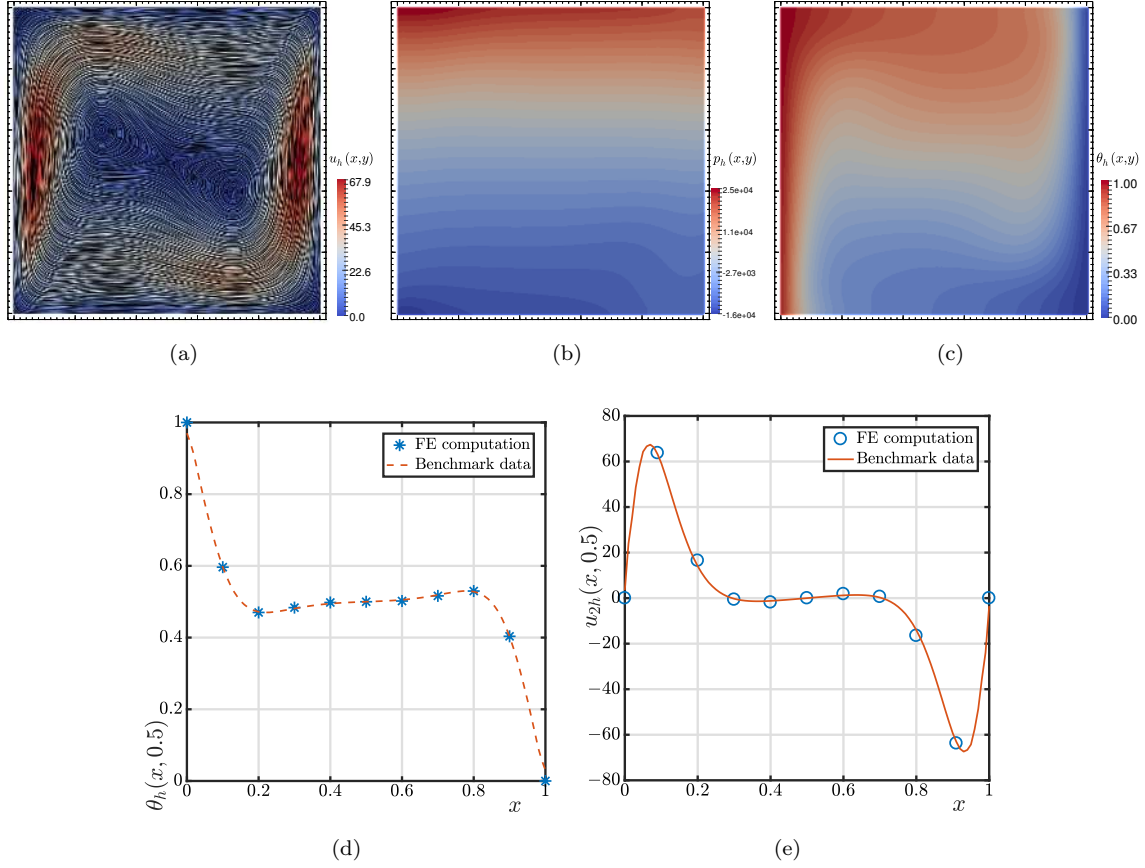


Figure 5.1: Velocity, pressure, and temperature profiles for the 2D differentially heated cavity (a,b,c respectively) and comparisons to the benchmark data in [36] (d and e).

of velocity, pressure and temperature distribution at the final time are depicted in Figure 5.1(a-c). We observe well-defined temperature profiles and the expected recirculation velocity patterns. A more quantitative study is done by extracting the approximate solutions for temperature and vertical velocity on the horizontal midlines at $y = 0.5$ and plotting them against properly rotated published benchmark values from [36] (which were generated using the method of discrete singular convolution). A reasonably close match is confirmed by looking at Figure 5.1(d,e), where we emphasise that our results come from coarse mesh computations.

	Ra	$\overline{\text{Nu}}$	$\max(\hat{u}_{1,h})$	$\max(\hat{u}_{2,h})$	x_∞	y_∞
Computed	10^3	1.105	0.133	0.137	0.177	0.815
Reference value	10^3	1.117	0.136	0.138	0.178	0.813
Computed	10^4	2.002	0.188	0.239	0.117	0.820
Reference value	10^4	2.054	0.192	0.234	0.119	0.823
Computed	10^5	4.430	0.161	0.258	0.068	0.851
Reference value	10^5	4.337	0.153	0.261	0.066	0.855

Table 3: Average Nusselt number (5.2) and maximum velocities on the midplanes attained at $(0.5, y_\infty)$ and $(x_\infty, 0.5)$, computed for different values of the Rayleigh number and compared with respect to reference values from [16].

We carry out further comparisons based on the average Nusselt number on the hot wall of the

cavity, that is, at $x = 0$. The value is here defined as

$$\overline{\text{Nu}} = \left| \int_M \text{Pr Re } u_1 \theta - \partial_x \theta \right|, \quad (5.2)$$

where M denotes the hot wall, and it encodes the rate of heat transfer along M (including the total flux, even the part coming from advection). We also record the maximum and minimum velocities and temperatures attained on the symmetry lines $x = 0.5$ and $y = 0.5$. The computed values are collected in Table 3, where we also include reference values from the literature.

6. The Melting of n-Octadecane

The melting of n-Octadecane has been numerically investigated by Danaila [14], the jump function for the enthalpy and viscosity terms are well chosen and the results are verified against experimental data. In this section we reintroduce the relevant parameters for this model, and define our own jump functions for enthalpy and viscosity. The jumps introduced are different to Danaila's own choice, the reason for this is that this section concerns itself with comparing the Enthalpy-Viscosity model of phase change to the Enthalpy-Porosity model of phase change, rather than producing results that reflect experimental data.

For the melting problem, we use the set up described by Danaila A two dimensional square, initially filled with solid phase change material (n-Octadecane), is subject to heating on the left hand side of the box.

Boundary conditions

For velocity, we impose the no slip condition $\mathbf{u} = 0$ on all container walls. We impose Dirichlet boundary conditions for temperature on the left and right hand side boundaries, θ_H and θ_C respectively. On the upper and lower plates we impose Neumann boundary conditions for temperature $\nabla \theta \cdot \mathbf{n} = 0$.

Initial conditions

Initially at $t = 0$ we have the initial conditions

$$\begin{aligned} \theta &= \theta_H & \text{on } \partial\Omega_L, \\ \theta &= \theta_C & \text{else.} \end{aligned}$$

We also set the initial temperature less than the melting temperature $\theta_C < \theta_f$ so that the phase change material is initially in mushy or solid form. Then heating from the left hand wall causes the melting of the phase change material.

Rate of change of Enthalpy

In a phase change system we have a term s representing enthalpy, and this form takes into account the energy needed to melt a solid. This has physical relevance and we include the term $\frac{\partial s}{\partial t}$, to model the time taken to melt the solid. This term would be worthy of inclusion in any model for physical modelling reasons alone, but an additional benefit of including the rate of change of enthalpy is that slowing down the melting front propagation increasing numerical stability. This is not obvious at all from the proof of uniqueness as the enthalpy term we introduce violates the conditions that ensure uniqueness.

Convection of Enthalpy

In the standard Enthalpy-Porosity model the term corresponding to the convection of enthalpy ($\mathbf{u} \cdot \nabla s$) is included. However when considering the viscosity model the convection of enthalpy is neglected, because the term ($\mathbf{u} \cdot \nabla s$) is only non-zero when we are in the mushy region, and the mushy region should be relatively small [14]. We will work with this assumption for both the Enthalpy-Viscosity model, and the Enthalpy-Porosity model.

Parameter Used	Value
penalty pressure constant γ	10^{-7}
Rayleigh number Ra	$3.27 * 10^5$
Prandtl number Pr	56.2
Reynolds number Re	1
Thermal conductivity K	1
Stephan number Ste	0.045
Left wall temperature θ_H	1
Cold Temperature θ_C	-0.01
Melting temperature θ_f	0.0
Mushy region $\delta\theta$	0.1

Numerical Parameters We will work with the parameters defined by the melting of n-Octadecane which we give in table.

Enthalpy

$s(\phi) = s_s + (s_l - s_s)\phi$, where $s_l = 0$, $s_s = [\text{Ste}]^{-1}$, accounts for the latent heat. ϕ is defined as in (3.4). But for constants given in the table. We define ϕ for additional clarity

$$\phi = \frac{1}{2}[\tanh(50\theta) + 1]. \quad (6.1)$$

The choice of ϕ highlights the difference between the Enthalpy–Viscosity model and the Enthalpy–Porosity model, and is not reflective of a particular physical experiment. The boundary condition on the cold wall is $\theta_c = -0.01$, and we regularise around 0 with a mushy region size 0.1 so we technically do not have a solid region, by the somewhat arbitrary definition of solid, $\phi < 0.01$ found in [32]. However, the jump is large enough so that the mushy region acts as a solid near the melting point. Danaila’s choice of jump function has a smaller mushy region and regularises around an artificial melting point, to avoid the notion of a liquid-mushy model.

6.1. The Enthalpy–Viscosity method

We let $\eta(\theta) = 0$ and $\mu(\theta)$ be a jump function that embeds the phase change, we use the viscosity jump defined by equation (3.8), with constants $\mu_l = 1$, $\mu_s = 10^8$, $M_\mu = 50$, $\theta_f = 0.0$. This form can also be regularised by ϕ as

$$\mu(\phi) = \mu_s + (\mu_l - \mu_s)\phi.$$

6.2. The Enthalpy–Porosity method

In the last subsection we saw the implementation of the enthalpy viscosity method to model the phase change in the melting of n-Octadecane. We now implement the Enthalpy–Porosity model with an almost identical jump. So we let $\mu(\theta) = 1$ and $\eta(\theta)$ is a jump function. We define $\eta(\theta)$ by the equation (3.5), with the numerical constants: $\eta_s = 10^8$, $M_\eta = 50$, $\theta_f = 0$. This can also be regularised by the same ϕ as,

$$\eta(\phi) = \eta_s(1 - \phi).$$

6.3. Numerical results

We implement the numerical methodology introduced in section 4. A Newton linearisation of equation (4.4) is introduced with a tolerance of 1E-6. The finite element spaces 4.1 are chosen with $k = 1$. We implement both methods described above to model a phase change subject to the

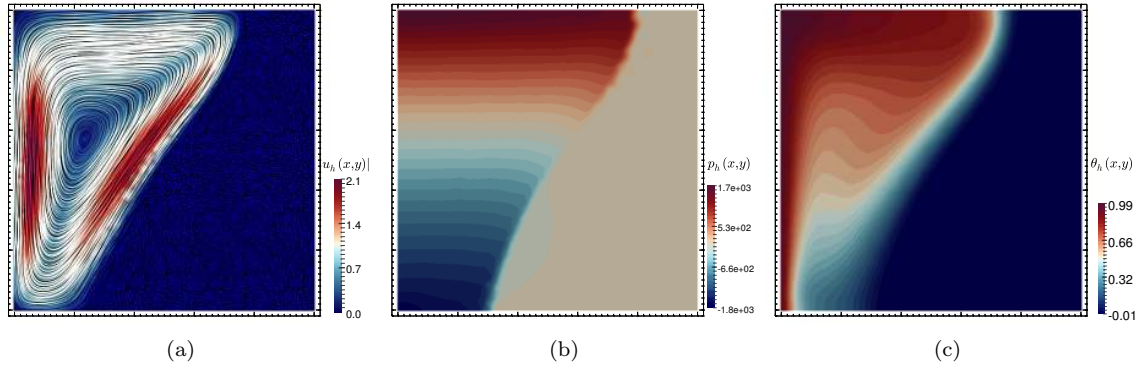


Figure 6.1: Velocity magnitude, pressure, and temperature profiles for the 2D differentially heated cavity (a,b,c respectively). For the Enthalpy-Viscosity model

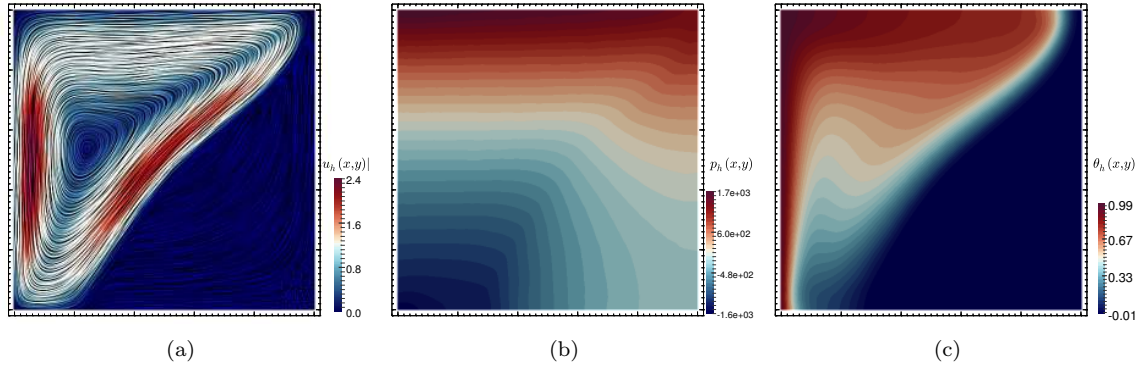


Figure 6.2: Velocity, pressure, and temperature profiles for the 2D differentially heated cavity (a,b,c respectively). For the Enthalpy-Porosity model

boundary conditions and numerical parameters relevant to the model given. We extract the profiles of the melting front defined by $\theta = 0$ at the adimensional time $t = 80$.

In Figure 6.1 we have the Enthalpy-Viscosity method and in Figure 6.2 we have the Enthalpy-Porosity method. The results are discussed next.

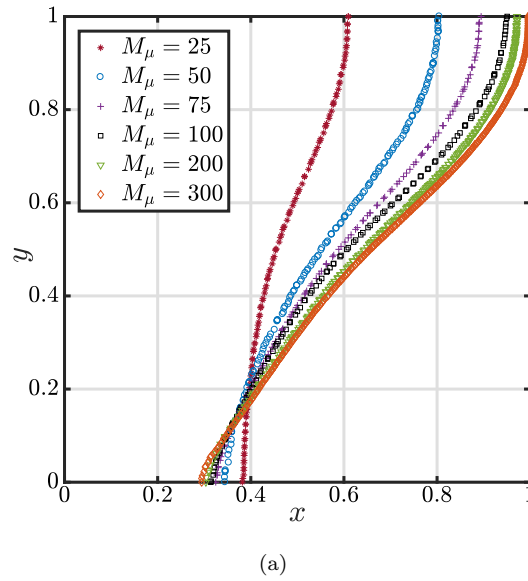
Comparison

We observe that the porosity model, behaves differently, upon an almost identical jump. Firstly we observe, the porosity model allows slight flow in the solid, this can be easily remedied by using a larger value for η_s . Secondly we observe, the phase change boundary is more advanced, and there is more advancement at the top of the container. The next section will attempt to explain why the contact line is more advanced.

7. Different Mushy Region sizes for the Enthalpy-Viscosity method

The Enthalpy-Viscosity method has been successfully used to model phase change in n-Octadecane [14]. The Enthalpy-Porosity method has been used to model solid liquid interfaces successfully [32]. However, implementation of both methods to the same jump function leads to different results. This section seeks an explanation of how to modify the Enthalpy-Viscosity model to match the result created by the Enthalpy-Porosity model.

R. Murray and D. Groulx[4] investigate how the enthalpy viscosity model is very sensitive to vari-

Figure 7.1: Enthalpy-Viscosity model with different values of M_μ

ous different parameters, including dynamic viscosity, thermal conductivity amongst various other parameters including mushy region size. P.W. Schroeder and G. Lube [32] observe that the Enthalpy-Porosity model is only physically realistic for the melting of gallium in a rectangular domain for a specific mushy region size. Both papers highlight that the results are very sensitive to the mushy region size. We hypothesise that altering the mushy region size, could allow the Enthalpy-Viscosity model to successfully match the Enthalpy-Porosity model.

We keep the enthalpy jump the same (regularised by $s(\phi) = s_s + (s_l - s_s)\phi$), while altering the constant M_μ in the viscosity jump (3.8) in the hope we can match the porosity model. We use mesh adaptivity to deal with the larger constants, or we don't get a convergent method.

Numerical results We continue to use the set up described in the previous section. We extract the melting front defined by $\theta = 0$ at the adimensional time $t = 80$ and plot them against each other for a range of values of M_μ . We present the results in Figure 7.1, and notice increasing the value M_μ leads to a more advanced contact line. We remember that M_μ is inversely proportional to the size of the mushy region $\delta\theta$, so we can think of these models in this respect. We also compare these melting fronts to those in Figure 6.1 and Figure 6.2 and note that the mushy region is a parameter that can make the models approximately equivalent provided the

Physical explanation

We present a possible physical interpretation to why the mushy region size has such a profound effect on the melting front. Making the mushy region smaller means that there is more liquid in the system, hence the amount of heat distributed through convection is drastically increased.

Conclusion

Given a larger value for M_μ the Enthalpy-Viscosity model can accurately mimic the Enthalpy-Porosity model, this is the main result of this project's numerical modelling. It is important to note that the smaller mushy region in the viscosity jump doesn't necessarily mean that the model has higher irregularity, the porosity jump needs to impose a larger jump to stop flow in the solid region. We note another important distinction, we needed mesh adaptivity for the higher values of M_μ to be convergent. This highlights that although the Enthalpy-Viscosity model can be modified to model a small mushy region, the Enthalpy-Porosity model incorporates it more naturally.

8. Jump forms arising from literature

In this section we introduce the numerical results of modelling the Carman-Kozeny equation (3.4). We introduce the model (3.7), and numerically model it for different choices of the parameter, n .

8.1. Carman-Kozeny form

When modelling the Enthalpy–Porosity model, it is common place to use a jump function coming from the literature on flow through packing beds; we use equation (3.4) with the constants $\xi = 10^{7.4}$, $m = 10^{-2.6}$. We have ϕ as previously defined (6.1). These constants are defined to have η regularised over the desired mushy region, with a higher constant than 10^8 in the solid region to reduce the flow in the solid.

We note that this form is roughly equivalent to the alternative jump form (3.5) with mushy region $M_\eta = 150$. This is a large value, especially considering the fact the porosity model doesn't need a mushy region so small, as compared to the viscosity model.

We refine near the phase boundary to deal with the increased irregularity of the jump function. We do this by adapting the mesh to the Hessian of temperature this is done using the adaptmesh function in FreeFem++. We re-mesh at every timestep, and use lots of small time steps, to ensure that the phase boundary remains in a region of h-refinement. This will in turn mean the Newton method will be in the zone of attraction, and we get convergence. The mesh refinement can be observed in Figure 8.1(e).

We do not get results close to experimental data [27]. This is because the constants ξ and m are chosen to regularise the equation over the required mushy region. It would be interesting to see the effects on how the Carman-Kozeny equation should be embedded, whether a different choice of these parameters would allow physically realistic modelling. We would require experimental values of ξ related to n-Octadecane, which I am yet to stumble upon. However I suspect that the accurate modelling of the experiment would not be achievable with the Enthalpy–Porosity model, partly because the Enthalpy–Porosity models naturally embeds a small mushy region and the Carman-Kozeny form even more so. Making the Carman-Kozeny equation more suited to materials that have more distinct liquid solid interfaces (explaining the success of this method of embedding a phase change in the melting of metals [32]), but not common in the literature on mantle convection where there are notions of larger mushy regions.

8.2. New Viscosity model

Recall equation(3.7)

$$\mu = \frac{1}{\phi^n + m}.$$

We choose $m = 10^{-8}$ to get the jump of order 10^8 . Plotting η against θ it is clear that we have to regularise ϕ differently to get the jump over the required region. For example with $n = 2.5$ we have to pick $\phi = \frac{1}{2}[\tanh(50(x - 0.074)) + 1]$ to get the jump over the required region. We now compute models for different values of n . In figure 8.2 we extract the usual melting front, obtained in the melting of n-Octadecane, described in section 6.

Conclusion This model can be successfully made to work, provided care is taken defining ϕ . It is based upon theory of how the packing density of a suspended particle solution effects viscosity. I haven't seen this model coupled to temperature to embed a phase change, and it works reasonably well and can match the Enthalpy–Porosity method.

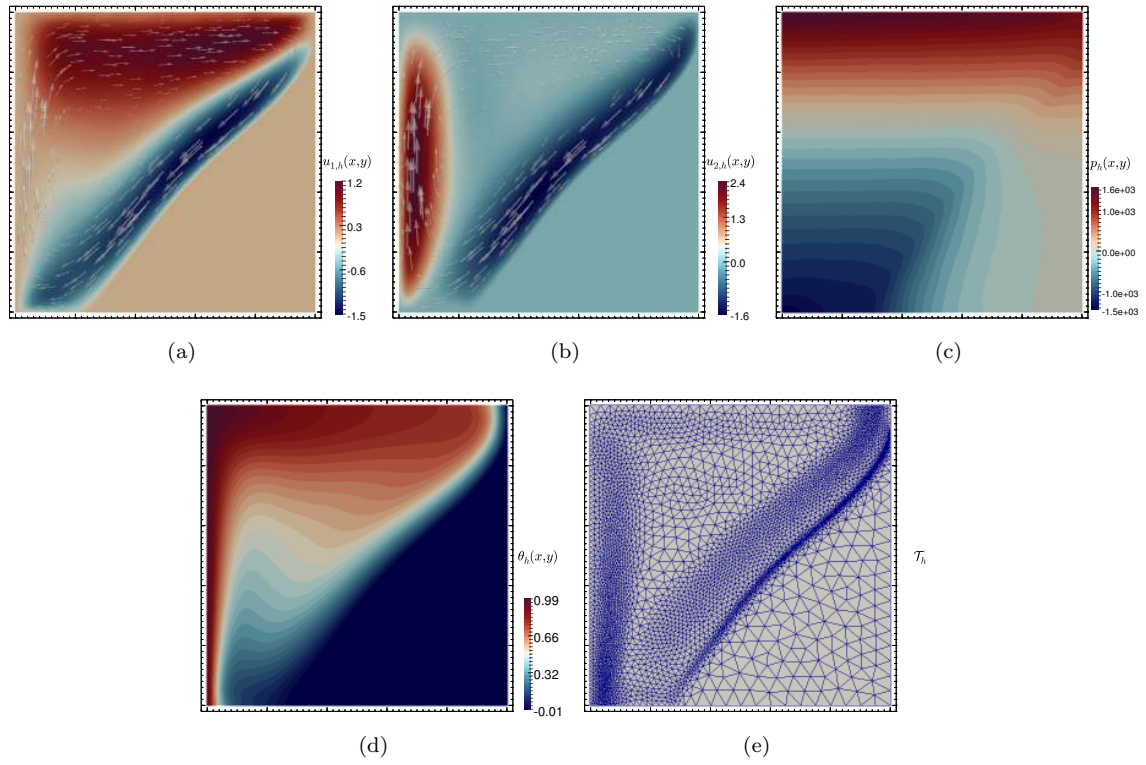


Figure 8.1: (a)(b) the velocity components, (c) pressure, (d) temperature profiles for the 2D differentially heated cavity with the Carman-Kozeny form for a phase change, with adaptive mesh near to phase boundary, (e)

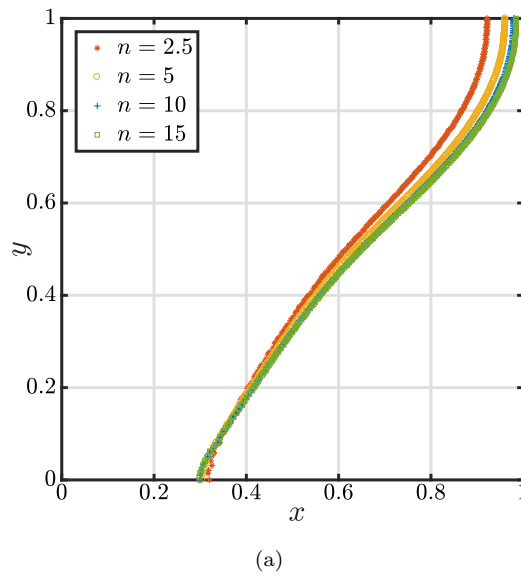


Figure 8.2: Comparison of the introduced model 3.7 with different values for n

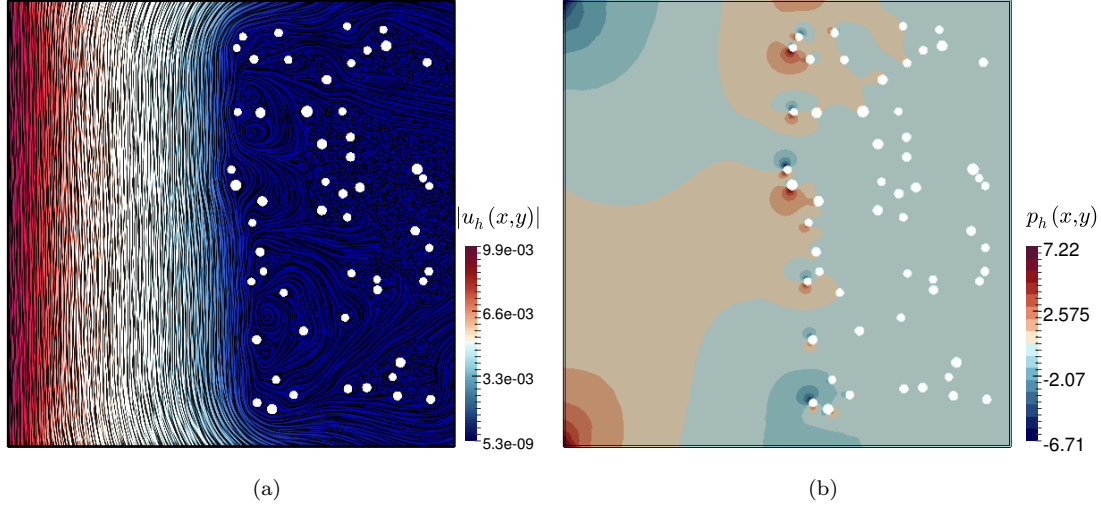


Figure 9.1: Cavity driven flow being slowed by imposed particles on a micro element

9. Intuition on the modelling

9.1. Local Element

In this section we introduce a small element on the phase boundary, governed by cavity driven flow. We use incompressible Navier-Stokes equations i.e. (3.1) and (3.2) where $\mu = 1$, $\eta = 0$, and $f = 0$. We represent the solid phase by creating a field of particles in the mesh itself; this will impose a drag force in the same way the Carman-Kozeny form does.

Mesh

We impose relatively sparse randomly distributed particles, with slight variance in diameter, centred around $d_m \approx 0.0002$.

Boundary conditions

$$\begin{aligned} \mathbf{u} &= (0, 0.01) \quad \text{on} \quad x = 0, \\ \mathbf{u} &= (0, 0) \quad \text{on} \quad \partial\Omega/(x = 0). \end{aligned}$$

Discussion of figure 9.1

Here the particles are fixed, and a drag force is imposed on the fluid as it tries to pass through the mesh. This is how the Carman-Kozeny jump form for porosity is considered. You can see that the velocity is reduced on a very small interval, but flow is allowed through the permeable field.

The viscosity models introduced from the literature on nanoparticle suspensions consider the effects with particles that move. We haven't computed a model where the particles are allowed to move, and occur only on the right hand side of the box, as it is computationally demanding. However it is reasonable to imagine that for the existing configuration on the micro-element, the flow on the right hand side of the container wouldn't be reduced as drastically. The particles couldn't induce as much resistance if they can be carried by the fluid. This gives us insight into why the viscosity formulation requires a much smaller mushy region to impose the same melting front.

Conclusion

The velocity is reduced drastically when approaching the imposed particles. This gives intuition on why the Carman-Kozeny form in particular and more generally the enthalpy-porosity model naturally imposes a small mushy region. This is why when we previously imposed the same jump

for Enthalpy–Porosity and Enthalpy–Viscosity, the Enthalpy–Porosity model had a more advanced contact line.

9.2. Similarity between forms

We discussed previously that the forms used in the Enthalpy–Porosity or the Enthalpy–Viscosity method, have relation to imposing particles in the fluid, fixed or moving respectively. Rodriguez [30] modifies the Carman-Kozeny form for porosity to

$$\eta = \xi \frac{(1 - \phi)^{n_1 - 1}}{\phi^{n_1}},$$

where n_1 and ξ are parameters, often chosen to match experimental data.

Now we consider the remarkable similar form coming from the viscosity modelling

$$\mu = \frac{1}{\phi^n},$$

where n is chosen to match experimental data.

When modelling a phase change the ϕ is regularised by a tanh jump function. The dominant term in the above two formulations is $\frac{1}{\phi^n}$. This n has an effect of effectively changing the mushy region size. So the literature indirectly highlights that the mushy region is an important factor for both porosity and viscosity modelling. We can modify the Carman-Kozeny and viscosity models, to incorporate a sharper jump form, which is equivalent to reducing the mushy region. This was actually the initial inspiration that made me think that the mushy region played a important role in the modelling.

We still note that naturally the porosity model embeds a smaller mushy region, this is an inherent property of how the jump is incorporated in the Boussinesq system. Advice to users wanting to implement a phase change. For a small mushy region, the Enthalpy–Porosity method is an effective way of stopping the flow. For a larger mushy region use the viscosity formulation. There are other considerations to take into account, this project shows that the models can be interchanged provided care is taken.

10. Modelling restrictions, and future modelling

In this section we look at a wide variety of numerical problems, where we not only describe a few systems in where the Boussinesq model discussed can be applied.

We first illustrate a more sophisticated viscosity formulation based on experimental data, and present an illustration of its use. We then implement a novel example of flow past an air foil, where we simplify the model considerably and note limitation of the continuous finite element methodology itself. We then model Rayleigh Taylor instability, highlighting the effect of salt on the flow of water. We then turn to a overly ambitious problem, modelling the flow of water as an ice sheet surrounding Antarctica melts. We describe that our model would allow the encoding of such a complicated physical system, but explain that even when we implement simplistic modelling we get computational difficulty treating a three dimensional model. We finally present illustrations on the Antarctica model but restricted to an unrealistic two dimensional model.

10.1. Viscosity Formulation, application; Mantle Convection

The viscosity dependence of suspended particles in solution has been the subject of scientific investigation and different models have been suggested. Antonio Costa introduces a different

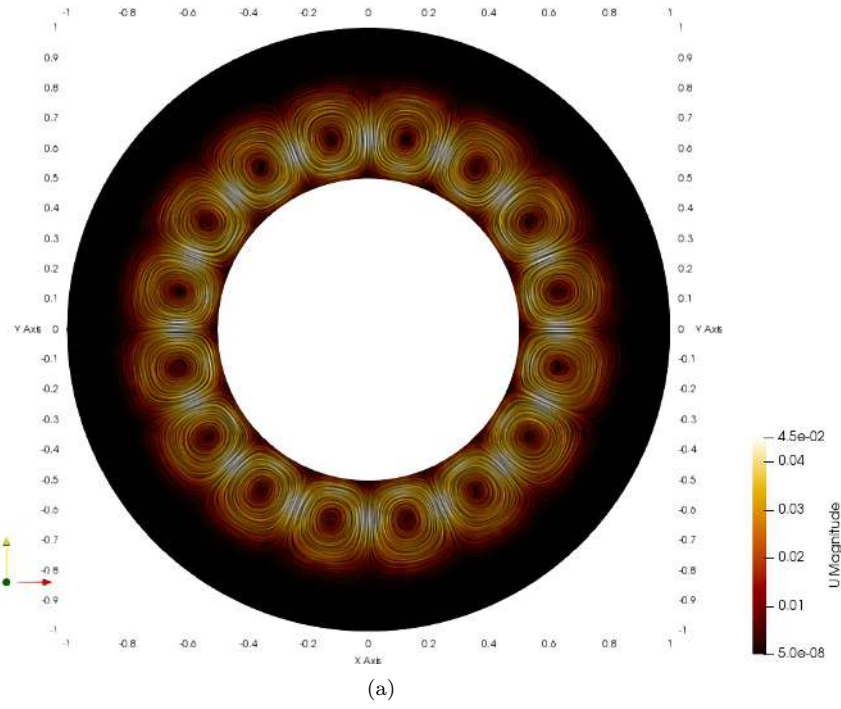


Figure 10.1: Mantle Convection: Convection, plays an important part in plate tectonics, as the convection of mantle is suggested as one of the reasons for tectonic plate movement. Above is an illustration on how the Enthalpy-Viscosity method can embed the phase change.

parametrisation of $\mu(\theta)$ based on the error function [13]

$$\mu(\Phi) = \left\{ 1 - \alpha \operatorname{erf} \left(\frac{\sqrt{\pi}}{2} \Phi \left[1 + \frac{\beta}{(1 - \Phi)^\gamma} \right] \right) \right\}^{-\frac{\beta}{\alpha}}.$$

It has different parameters that allow the matching of experimental data and has been shown to accurately match viscosity data for high and low crystal content melts. We introduce a particular choice of parameters $\alpha = 0.9995$, $\beta = 0.4$, $\gamma = 1$, $\phi_c = 0.55$ [13] are chosen with a maximum attainable value of $\mu_{\max} = 1.8 \times 10^8$, and the model matches observed experimental values of the viscosity of magma produced in [37] while also matching numerical values of Thomas [1965][34] at low liquid fraction. This gives motivation into coupling temperature with liquid fraction as before to model mantle flow. Although modelling with this form has relation to packing particles, we are yet to compute a physically realistic model. An interesting extension for this project would be to try and reproduce some of the results found in [35]. We have defined the correct model to do such a task, all that needs embedding is the boundary conditions and correct parameters.

In our numerical illustration 10.1, we embed a simple viscosity jump of the form (3.8). We do not use realistic parameters or initial conditions, but we do use the equations (3.1) (3.2) (3.3) with $\eta = 0$. Instead we have an illustrative model in Figure 10.1 where we observe Bernard convection rolls in the magma and very little flow on the crust of the Earth.

10.2. Increasing sensitive parameter and the limitation of the finite element method; Plane Wing

Here we demonstrate FreeFem++ meshing capabilities with a novel example, low Mach number flow of an air-foil. Blaze Gardner at Sheffield Hallam University, has been building the NACA-SC-0712 air foil, to run through an air tunnel at low speeds. We turn the image into a mesh, using the

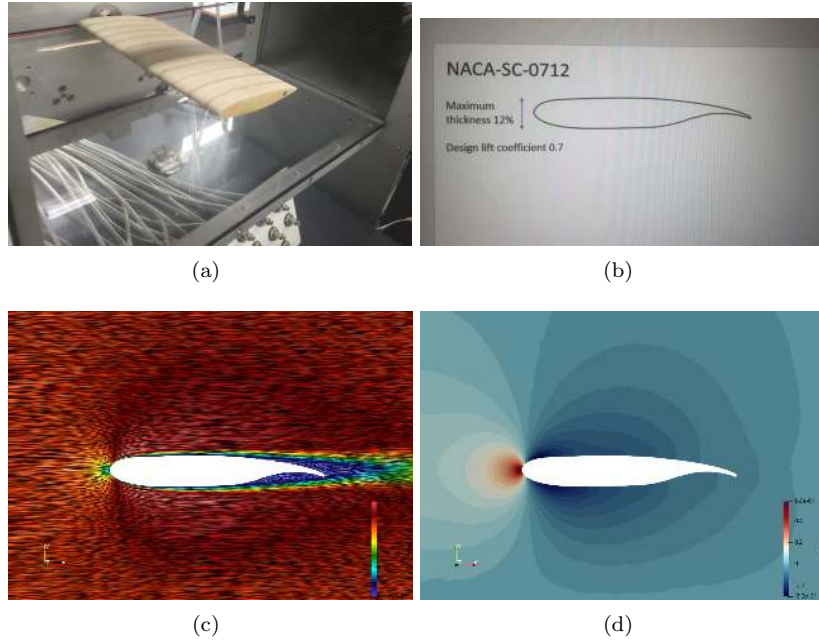


Figure 10.2: Airfoil in a wind tunnel (a), and its ideal shape, (b). Velocity and temperature profiles for flow around NACA-SC-0712 air foil (c,d respectively).

isoline and buildmesh capabilities in FreeFem++. Since the experiment he is working on is at low Mach number < 0.3 we can model the experiment as the steady state incompressible Navier-Stokes equations. More explicitly we work with the equations (3.1), (3.2) where $\mu = 1$, $\eta = 0$ and $f = 0$. We produce velocity and pressure images for the solution of Navier-Stokes at $Re = 10^4$ in Figure 10.2.

This is discussed to show how convergence with difficult parameters can be achieved; we observed high Reynolds numbers are hard to get to converge. To get convergence we use a stepping technique, using the solution to the low Reynolds flow as initial conditions for the Picard method until we are in the radius of convergence, then use the Newton method to converge to the correct solution for a higher Reynolds number. This is repeated until convergence of the required Re , this method is suggested in [21]. Later in this section we will introduce the model for the melting of an ice sheet surrounding Antarctica, where we use a stepping technique to get larger parameters for Rayleigh number Ra , see Figure 10.6. The Rayleigh number is a sensitive parameter to increase for thermally driven flow [32].

In practice the finite element method will fail when considering advection dominated problems, and the model itself breaks down, as the flow becomes compressible and shock waves form. Finite volume methods, and discontinuous finite element methods are needed to deal with fast airflow problems. The choice of Reynolds number as 1000 we managed to get to converge corresponds to slow flow through air, the onset of turbulence occurs at approximately this order of Reynolds number, where the model and numerical methods are destined to fail.

10.3. Rayleigh Taylor instability

Two approximately immiscible fluids of different densities are in a container. The denser fluid is placed on top of the less dense fluid. We model this by having the incompressible Navier-Stokes with a linear buoyancy force coupled with the advection-diffusion equation where we choose advection dominated flow. This model is the same as (3.1) (3.2) (3.3) where we let $\theta = \varsigma$ be the concentration of salt, $\mu = 1$, $\eta = 0$, $Re = 1$ and we have no enthalpy terms in the equation (3.3). The advection diffusion equation represents the distribution in salt, that causes the densities of the liquid to differ

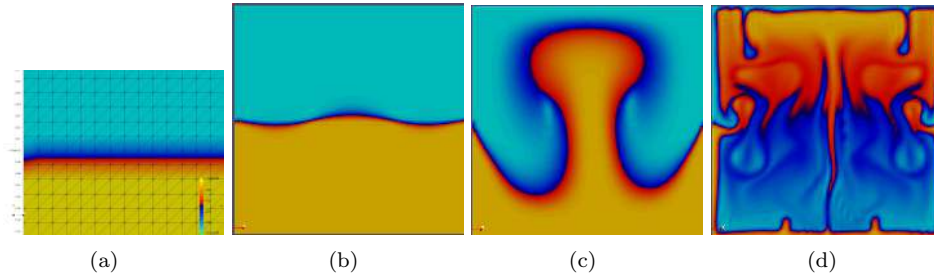


Figure 10.3: a) Tiny perturbation on left boundary. (b)(c)(d) are images of Rayleigh Taylor instability progressing. In (d) you observe slight asymmetry caused by the tiny perturbation in (a), or possibly from the numerical approximations.

and this is accounted for by the introduction of a linear buoyancy term that causes flow. For the Figure 10.3 we choose to demonstrate the effect when the liquids are approximately immiscible so we pick CPr as a very small constant.

Some systems are deterministic in nature but are extremely sensitive to initial conditions. We introduce this example because the solution should be symmetrical, however we have a tiny perturbation initially near the side wall that amplifies 10.3.

With regards to future modelling, we may have results that inherit solutions based upon the choice of spacial discretisation, numerical approximation errors give largely different solutions. With this sort of behaviour qualitatively discussed we turn to modelling flow near Antarctica, where we may have the "underwater butterfly effect".

10.4. Antarctica

Here we discuss the modelling of fluid flow around Antarctica as an ice sheet melts. We consider the 3d fluid space around Antarctica. We have double diffusive natural convection, as salt and temperature effect the buoyancy of water. We have a phase change to encode in the formulation. We have various other modelling considerations to take into account, currents and winds, the effect of ice melting giving off cold fresh water, the varying density of the fluid, the initial conditions and boundary conditions and realistic parameters. Despite the increased complexity of the modelling described, it could in theory be modelled by the methods introduced in this project.

We attempt to implement a simple model, where many effects are neglected. A three dimensional mesh can easily be created using the *medit* extension of *FreeFem++*, after identifying the largest contour in the png image and turning this into a mesh, meshing process illustrated in Figure 10.4. We then choose to embed a phase change with the viscosity formulation, to model an ice sheet initially defined on the upper surface of the 3d model. We prescribe boundary conditions that are cold on Antarctica and hot on the equator. Then we attempt to solve the phase change Boussinesq system, with the very relaxed modelling assumptions. The linear solver couldn't deal with the size of the matrix generated, the practical solution of a three dimensional problem is computationally way too demanding, most high resolution three dimensional computations rely on computers more powerful than a laptop.

So instead we present an illustrative two dimensional image representing a solution of the flow, near a melting ice sheet surrounding Antarctica. We use simplified modelling assumptions, and hence refer to the images created as illustrations as they will not reflect the real three dimensional model.

We observe the melting of an ice sheet and the fluid flow resulting from this, in the model in Figure 10.5. We implement a higher Rayleigh number, in 10.6 and do not embed a phase change.

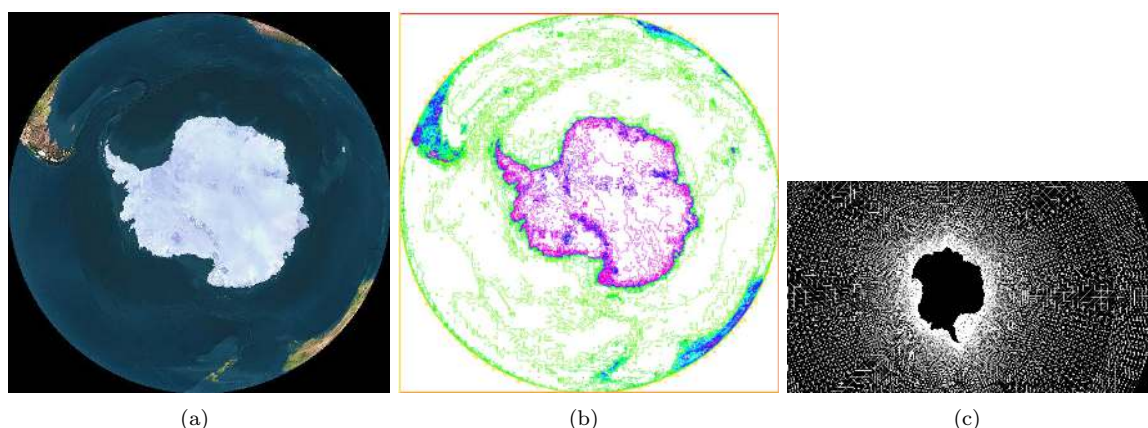


Figure 10.4: (a) Image of Antarctica from Google Earth, (b) png image, where the contour of Antarctica is in blue, (c) The 3D mesh generated.

11. Conclusion

We have addressed the modelling of phase change in Boussinesq models within porous media. A finite element method has been proposed for the numerical approximation of the method, and we have established stability of the scheme. We have tested the performance of the method using a classical benchmark for air convection.

We have successfully applied numerical methods for the Enthalpy–Viscosity model and the Enthalpy–Porosity model observed different results for a similar jump function and drawn an equivalence between the models by identifying the parameters that need to be considered to get similar numerical results. This result is important because now those wishing to embed a phase change can change between the two models. This has application in modelling and functional analysis of Boussinesq phase change models.

We then model the Enthalpy–Viscosity and the Enthalpy–Porosity model with jump functions arising from literature on how particles and porosity effect the flow of a liquid. The form we use for viscosity has never been used to embed a phase change as it has never been coupled with temperature. In section 2 we introduce the literature used to arrive at the model. Similar to before we identify a parameter in the new viscosity model that can be varied to match the porosity model. We discuss the difference between models of phase change and impose a mesh to mimic the effects of the Carman-Kozeny form.

The aims of the project are achieved and future directions and modelling restrictions, are addressed.

12. References

- [1] R. AGROUM, C. BERNARDI, J. SATOURI, *Spectral discretization of the time-dependent Navier–Stokes problem coupled with the heat equation*. Appl. Math. Comp., 268 (2015), 59–82.
- [2] H. ABBOUT, V. GIRAULT, T. SAYAH, *A second order accuracy for a full discretized time-dependent Navier–Stokes equations by a two-grid scheme*. Numer. Math., 114 (2009), 189–231.
- [3] M. ALVAREZ, B. GOMEZ, R. RUIZ-BAIER, J. WOODFIELD, *Numerical solution of a phase-change model for natural convection in porous media*. Unpublished.
- [4] S. ARENA, E. CASTI, J. GASIA, L.F. CABEZA, G. CAU, *Numerical simulation of a finned-tube LHTES system: influence of the mushy zone constant on the phase change behaviour*. Energy Procedia 126 (2017) no. 09, 517–524.

- [5] C. BECKERMANN, R. VISKANTA, *Natural convection solid/liquid phase change in porous media*. Int. J. Heat Mass Transf., 31 (1988), no. 1, 35–46.
- [6] A.D. BRENT, V.R. VOLLER, K.J. REID, *Enthalpy-porosity technique for modeling convection-diffusion phase change: application to the melting of a pure metal*. Numer. Heat Transfer, 13 (1988), no. 3, 297–318.
- [7] H.C. BRINKMAN, *The viscosity of concentrated suspensions and solutions*, J. Chem. Phys., 20 (1952), 571.
- [8] J. BOLAND, W. LAYTON, *An analysis of the finite element method for natural convection problems*. Numer. Methods Partial Diff. Eqns., 2 (1990), 115–126.
- [9] J. BOUSSINESQ, *Théorie de l'écoulement tourbillonnant et tumultueux des liquides dans les lits rectilignes a grande section*. Gauthier-Villars et fils, 1897.
- [10] P.C. CARMAN, *Fluid flow through granular beds*. Trans. Inst. Chem. Engr. London 15 (1937), 150–166.
- [11] P. G. CIARLET, *On Korn's Inequality*. Chin. Ann. Math. 31B(5), (2010), 607618.
- [12] A. CIBIK S. KAYA, *Finite element analysis of a projection-based stabilization method for the Darcy-Brinkman equations in double-diffusive convection*. J. Math. Anal. Appl. 381 (2011) 469–484
- [13] A. COSTA, *Viscosity of high crystal content melts: Dependence on solid fraction*. Geophys. Res. Letters, 32 (2005) no. 22.
- [14] I. DANAILA, R. MOGLAN, F. HECHT, S. LE MASSON, *A Newton method with adaptive finite elements for solving phase-change problems with natural convection*. J. Comput. Phys., 274 (2014), 826–840.
- [15] RIM EL DBAISSY , FRDRIC HECHT, GIHANE MANSOUR, TONI SAYAH. , *A full discretisation of the time-dependent Boussinesq (buoyancy) model with nonlinear viscosity*. 2017. [halshs-01646611v2](#)
- [16] G. DE VAHL DAVIS, *Natural convection of air in a square cavity: A benchmark numerical solution*. Int. J. Numer. Meth. Fluids, 3 (1983), no. 3, 249–264.
- [17] J. DETEIX, A. JENDOUBI, D. YAKOUBI, *A coupled prediction scheme for solving the Navier–Stokes and convection-diffusion equations*. SIAM J. Numer. Anal., 52 (2014), no. 5, 2415–2439.
- [18] N.S. DHAIDAN, J. KHODADADI, T.A. AL-HATTAB, S.M. AL-MASHAT, *Experimental and numerical study of constrained melting of n-Octadecane with CuO nanoparticle dispersions in a horizontal cylindrical capsule subjected to a constant heat flux*. Int. J. Heat Mass Transfer, 67 (2013), 523–534.
- [19] A. EINSTEIN, *Eine neue Bestimmung der Molekuldimensionen*, Ann. Physik, 19 (1906), 286–306.
- [20] K. ENSSLIN, *Quantum physics in quantum dots. Nanophysics: Coherence and transport*. École d'été de Physique des Houches, Session LXXXI Les Houches, (2005) 585–586.
- [21] H.C. ELMAN, D.J. SILVESTER, A.J. WATHEN, *Finite Elements and Fast Iterative Solvers: with Applications in Incompressible Fluid Dynamics*, second ed., Oxford University Press, 2014.
- [22] V. GIRAULT, AND P. RAVIART, *Finite element approximation of the Navier-Stokes equations*. Berlin: Springer-Verlag, (2008).
- [23] J. KOZENY, *Ueber kapillare Leitung des Wassers im Boden*. Sitzungsber Akad. Wiss. Wien, 136 (1927), no. 2a, 271–306.
- [24] I.M. KRIEGER, T.J. DOUGHERTY, *A mechanism for non-Newtonian flow in suspension of rigid spheres*, Trans. Soc. Rheol., 3 (1959), 137–152.
- [25] J. L. LIONS, *Equations Dierentielles Operationnelles et Probl'emes aux Limites*. Springer-Verlag, Berlin, 1961.
- [26] H. MADER, E. LLEWELLIN, S. MUELLER, *The rheology of two-phase magmas: A review and analysis*. J. Volc. Geotherm. Res., 257 (2013), 135–158.

- [27] M. OKADA, *Analysis of heat transfer during melting from a vertical wall*, Int. J. Heat Mass Transfer, Vol 27, No. II, (1984) 2057–2066.
- [28] A. QUARTERONI, A. VALLI, *Numerical Approximation of Partial Differential Equations*. Springer Series in Computational Mathematics, vol. 23, Springer-Verlag Berlin Heidelberg, 1994.
- [29] H.M. QUINN, *A reconciliation of packed column permeability data: Column permeability as a function of particle porosity*. J. Materials (2014), 636507.
- [30] E. RODRIGUEZ, F. GIACOMELLI AND A. VAZQUEZ, *Permeability-Porosity Relationship in RTM for Different Fiberglass and Natural Reinforcements*. Journal of COMPOSITE MATERIALS, Vol. 38, No. 03/ (2004)
- [31] R. ROSCOE, *The viscosity of suspensions of rigid spheres*, Brit. J. Appl. Phys., 3 (1952), 267–269.
- [32] P.W. SCHROEDER, G. LUBE, *Stabilised dG-FEM for incompressible natural convection flows with boundary and moving interior layers on non-adapted meshes*. J. Comput. Phys., 335 (2017), 760–779.
- [33] R. TEMAM, *Une méthode d'approximation des solutions des équations de Navier–Stokes*. Bull. Soc. Math. France, 98 (1968), 115–152.
- [34] D. G. THOMAS, *Transport characteristics of suspension: 8. A note on the viscosity of Newtonian suspensions of uniform spherical particles*. J. Colloid Sci. 20:267277, (1965)
- [35] M. ULVROVÁ, S. LABROSSE, N. COLTICE, P. RØABACK, P.J. TACKLEY, *Numerical modelling of convection interacting with a melting and solidification front: Application to the thermal evolution of the basal magma ocean*. Phys. Earth Planet. Inter. 206–207 (2012), 51–66.
- [36] D.C. WAN, B.S.V. PATNAIK, G.W. WEI, *A new benchmark quality solution for the buoyancy-driven cavity by discrete singular convolution*. Numerical Heat Transfer B, 40 (2001), 199–228.
- [37] I. VAN DER MOLEN AND M.S. PATERSON *Experimental Deformation of Partially-Melted Granite*.

13. Appendix

13.1. Appendix A

We prove the first line in the uniqueness proof, in hopefully sufficient detail, for those uninitiated in proofs of this nature.

We consider the difference between two solutions of 3.16

$$\begin{aligned} & \left[(\partial_t[\theta_1 + s(\theta_1)], \psi) + c_3(\mathbf{u}_1; \theta_1 + s(\theta_1), \psi) + a_3(\theta_1, \psi) \right] \\ & - \left[(\partial_t[\theta_2 + s(\theta_2)], \psi) + c_3(\mathbf{u}_2; \theta_2 + s(\theta_2), \psi) + a_3(\theta_2, \psi) \right] = 0 \end{aligned}$$

we then consider grouping like terms, taking advantage of linearity where possible. We also define $\psi = \theta_1 - \theta_2 + s(\theta_1) - s(\theta_2)$, $\bar{\mathbf{u}} = \mathbf{u}_1 - \mathbf{u}_2$, $\bar{p} = p_1 - p_2$ and $\bar{\theta} = \theta_1 - \theta_2$ for ease of notation.

$$\begin{aligned} & (\partial_t[\psi], \psi) + \left[c_3(\mathbf{u}_1; \theta_1 + s(\theta_1), \psi) - c_3(\mathbf{u}_2; \theta_1 + s(\theta_1), \psi) \right] \\ & \left[c_3(\mathbf{u}_2; \theta_1 + s(\theta_1), \psi) - c_3(\mathbf{u}_2; \theta_2 + s(\theta_2), \psi) \right] + a_3(\bar{\theta}, \psi) = 0 \end{aligned}$$

$$\frac{1}{2} \frac{d}{dt} \|\psi\|_{0,\Omega}^2 + c_3(\bar{\mathbf{u}}; \theta_1 + s(\theta_1), \psi) + c_3(\mathbf{u}_2; \psi, \psi) + a_3(\bar{\theta}, \psi) = 0$$

use $c_3(\mathbf{u}_2; \psi, \psi) = 0$

$$\frac{1}{2} \frac{d}{dt} \|\psi\|_{0,\Omega}^2 + a_3(\bar{\theta}, \bar{\theta}) = a_3(\bar{\theta}, -(s(\theta_1) - s(\theta_2))) - c_3(\bar{\mathbf{u}}; \theta_1 + s(\theta_1), \psi)$$

then we take absolute value of the right hand side.

$$\frac{1}{2} \frac{d}{dt} \|\psi\|_{0,\Omega}^2 + \frac{\kappa_0}{CP_r} |\bar{\theta}|_{1,\Omega} \leq |a_3(\bar{\theta}, -(s(\theta_1) - s(\theta_2)))| + |c_3(\bar{\mathbf{u}}; \theta_1 + s(\theta_1), \psi)|$$

have to use lemma 3.3 for c_3 when we have that

$$\frac{1}{2} \frac{d}{dt} \|\psi\|_{0,\Omega}^2 + \frac{\kappa_0}{CP_r} |\bar{\theta}|_{1,\Omega} \leq \frac{\kappa_1 L_{s_2}}{CP_r} \int_{\Omega} \nabla \bar{\theta} |\bar{\theta}| + \|\bar{\mathbf{u}}\|_{4,\Omega} |\theta_1 + s(\theta_1)|_{1,\Omega} \|\psi\|_{4,\Omega}$$

using Cauchy-Schwarz and then

$$\frac{1}{2} \frac{d}{dt} \|\psi\|_{0,\Omega}^2 + \frac{\kappa_0}{CP_r} |\bar{\theta}|_{1,\Omega} \leq \frac{\kappa_1 L_{s_2}}{CP_r} |\bar{\theta}|_{1,\Omega} \|\bar{\theta}\|_{0,\Omega} + \|\bar{\mathbf{u}}\|_{4,\Omega} |\theta_1 + s(\theta_1)|_{1,\Omega} \|\psi\|_{4,\Omega}$$

13.2. Appendix B

We define the matrix system we solve numerically. As it may be useful to note the form.

Defining the basis functions that span the finite dimensional spaces $(\mathbf{V}_h, \mathbf{Q}_h, \mathbf{Z}_h)$ as $\{\phi_j\}, \{\psi_k\}, \{\gamma_\iota\}$ respectively. Then we have since the basis functions span the discrete space we can define,

$$\begin{aligned} \mathbf{u}_h^k &= \sum_{j=1}^{n_u} \mathbf{u}_j \phi_j + \sum_{j=n_u+1}^{n_{\partial \mathbf{u}}} \mathbf{u}_j \phi_j \\ \delta \mathbf{u}_h &= \sum_{j=1}^{n_u} \Delta \mathbf{u}_j \phi_j \\ \mathbf{v}_h &= \sum_{\hat{j}=1}^{n_u} \mathbf{v}_{\hat{j}} \phi_{\hat{j}} + \sum_{\hat{j}=n_u+1}^{n_{\partial \mathbf{v}}} \mathbf{v}_{\hat{j}} \phi_{\hat{j}} \\ p_h^k &= \sum_{k=1}^{n_p} p_k \psi_k \\ \delta p_h &= \sum_{k=1}^{n_p} \Delta p_k \psi_k \\ q_h &= \sum_{\hat{k}=1}^{n_q} q_{\hat{k}} \psi_{\hat{k}} \\ \theta_h^k &= \sum_{\iota=1}^{n_\theta} \theta_\iota \gamma_\iota + \sum_{\iota=n_\theta+1}^{n_{\partial \theta}} \theta_\iota \gamma_\iota \\ \delta \theta &= \sum_{\iota=1}^{n_\theta} \Delta \theta_\iota \phi_\iota \\ \psi_h &= \sum_{\hat{\iota}=1}^{n_\psi} \psi_{\hat{\iota}} \gamma_{\hat{\iota}} + \sum_{\hat{\iota}=n_\psi+1}^{n_{\partial \psi}} \psi_{\hat{\iota}} \gamma_{\hat{\iota}} \end{aligned}$$

For the implicit euler method we have the matrix system:

$$\begin{bmatrix} \frac{U}{\Delta t} + N + W + \frac{M}{\text{Re}} + \Lambda, & B^T, & H + \frac{T}{\text{Re}} + \Xi \\ B, & -\gamma Q, & 0 \\ -\widehat{W}, & 0, & \frac{\Theta}{\Delta t} + \frac{K}{P_r} Z - \widehat{N} + \frac{\widehat{\Theta}}{\Delta t} \end{bmatrix} \begin{bmatrix} \Delta \mathbf{u} \\ \Delta p \\ \Delta \theta \end{bmatrix} = \begin{bmatrix} F \\ G \\ H \end{bmatrix}$$

For the BFD-2 method we have the matrix system:

$$\begin{bmatrix} \frac{3U}{2\Delta t} + N + W + \frac{M}{\text{Re}} + \Lambda, & B^T, & H + \frac{T}{\text{Re}} + \Xi \\ B, & -\gamma Q, & 0 \\ -\widehat{W}, & 0, & \frac{3\Theta}{2\Delta t} + \frac{K}{P_r} Z - \widehat{N} + \frac{3\widehat{\Theta}}{2\Delta t} \end{bmatrix} \begin{bmatrix} \Delta \mathbf{u} \\ \Delta p \\ \Delta \theta \end{bmatrix} = \begin{bmatrix} f \\ g \\ h \end{bmatrix}$$

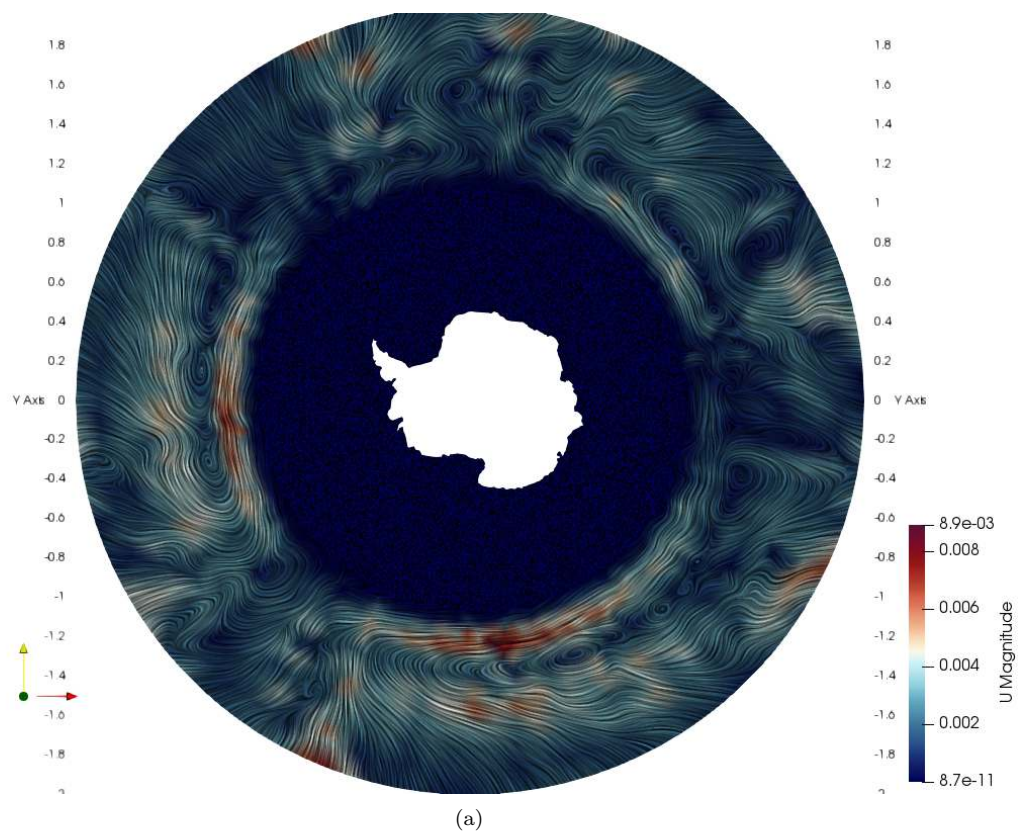
These matrix systems are solved at every newton iteration, until convergence. Where

$$\begin{aligned}
U &= \int \phi_j \cdot \phi_{\hat{j}}, \\
N &= \int [(u_h^k \cdot \nabla) \phi_j] \cdot \phi_{\hat{j}}, \\
W &= \int [(\phi_j \cdot \nabla) u_h^k] \cdot \phi_{\hat{j}}, \\
M &= \int 2\mu(\theta_h^k) \epsilon(\phi_j) : \epsilon(\phi_{\hat{j}}), \\
T &= \int 2 \frac{d\mu}{d\theta} \Big|_{\theta_h^k} \gamma_\iota \epsilon(u_h^k) : \epsilon(\phi_{\hat{j}}), \\
B^T &= - \int (\nabla \cdot \phi_{\hat{j}}) \psi_k, \\
B &= - \int (\nabla \cdot \phi_j) \psi_{\hat{k}}, \\
H &= - \int \frac{df}{d\theta} \Big|_{\theta_h^k} \gamma_\iota (\mathbf{k} \cdot \phi_{\hat{j}}), \\
\hat{N} &= \int (u_h^k \cdot \nabla) \gamma_\iota, \\
\widehat{W} &= \int [(\phi_j \cdot \nabla) u_h^k] \cdot \phi_{\hat{j}}, \\
Z &= \int \nabla \gamma_\iota \cdot \nabla \gamma_{\hat{\iota}}, \\
\hat{\Theta} &= \int \frac{ds}{d\theta} \Big|_{\theta_h^k} \gamma_\iota \gamma_{\hat{\iota}}, \\
\Lambda &= \int \eta(\theta_h^k) \phi_j \cdot \phi_{\hat{j}}, \\
\Xi &= \int \frac{d\eta}{d\theta} \Big|_{\theta_h^k} \gamma_j (u_h^k \cdot \phi_{\hat{j}}), \\
\Theta &= \int \gamma_\iota \cdot \gamma_{\hat{\iota}}.
\end{aligned}$$

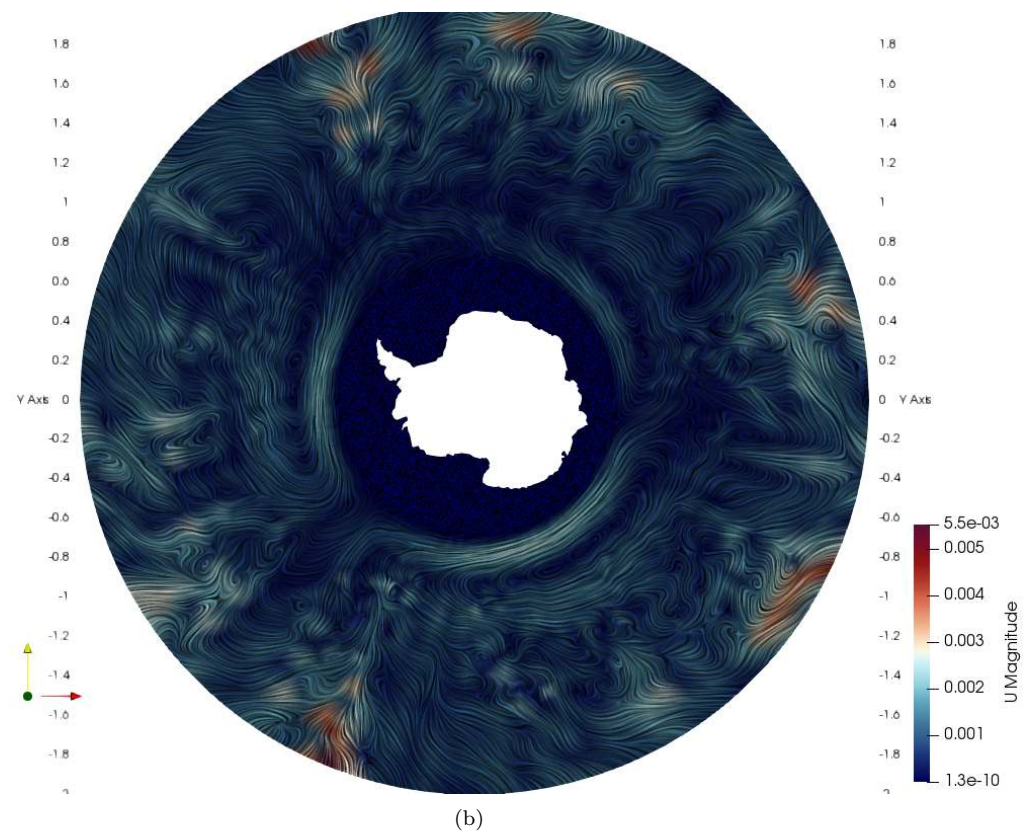
The forms for f, g, h and F, G, H are complicated forms, dependent on terms from; the residual arising from the Newton method, the boundary conditions and the previous time steps.

We observe that both phase change models have a similar effect on the matrix structure, which is as expected.

A future direction for the project would be preconditioning the matrix system. A possible strategy would be implementing a block matrix to take advantage of the velocity pressure schur matrix, which itself should be approximated by say the least squares commutator approximations. This may allow increased computation speed.

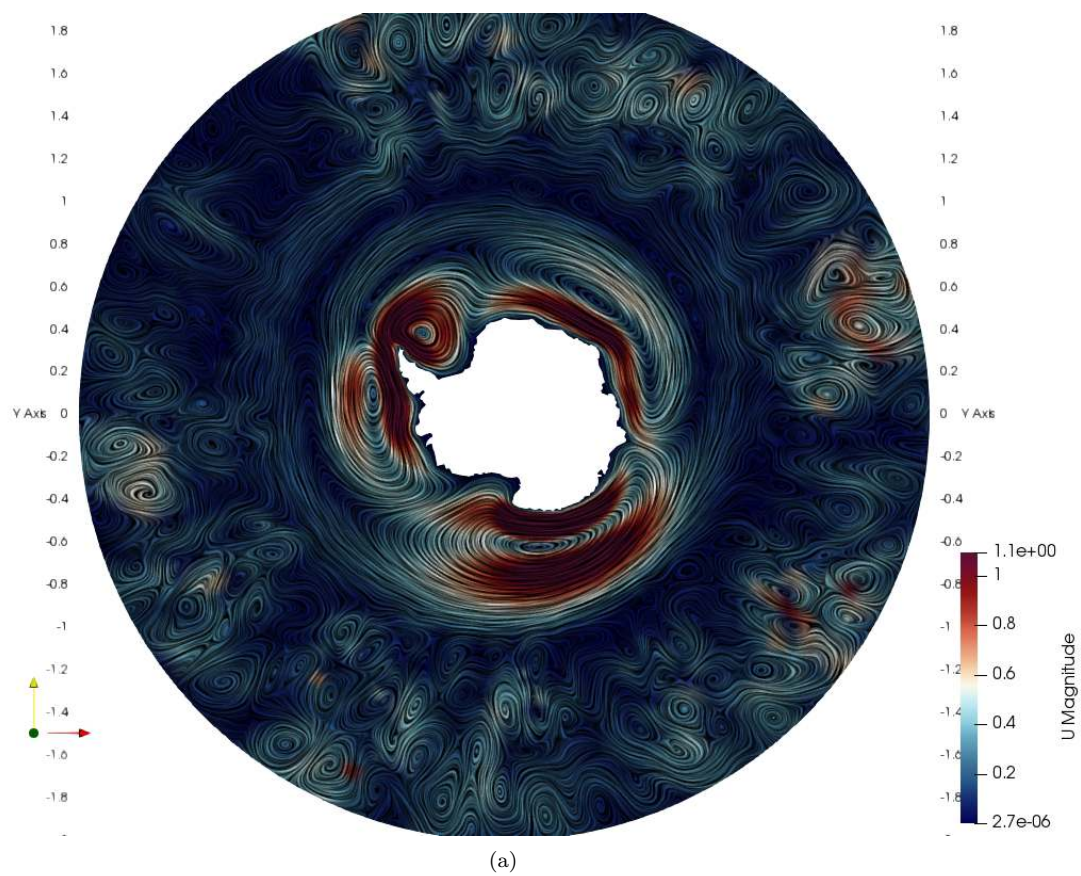


(a)



(b)

Figure 10.5: Melting case of Antarctica, .



(a)

Figure 10.6: Effect of a higher Rayleigh number, no phase change embedded.